

## RESEARCH ARTICLE

10.1002/2015JC010740

## Key Points:

- Thermal response to meteorological forcing of Lake Superior is examined
- Key to the modeling success is to resolve the lake-air interactions
- Spatiotemporal variability of surface meteorological components is important

## Supporting Information:

- Supporting Information S1

## Correspondence to:

P. Xue,  
pexue@mtu.edu

## Citation:

Xue, P., D. J. Schwab, and S. Hu (2015), An investigation of the thermal response to meteorological forcing in a hydrodynamic model of Lake Superior, *J. Geophys. Res. Oceans*, 120, 5233–5253, doi:10.1002/2015JC010740.

Received 20 JAN 2015

Accepted 10 JUN 2015

Accepted article online 23 JUN 2015

Published online 31 JUL 2015

## An investigation of the thermal response to meteorological forcing in a hydrodynamic model of Lake Superior

Pengfei Xue<sup>1</sup>, David J. Schwab<sup>2,3</sup>, and Song Hu<sup>4</sup>

<sup>1</sup>Department of Civil and Environmental Engineering and Great Lakes Research Center, Michigan Technological University, Houghton, Michigan, USA, <sup>2</sup>Michigan Tech Research Institute and Great Lakes Research Center, Michigan Technological University, Ann Arbor, Michigan, USA, <sup>3</sup>University of Michigan Water Center, University of Michigan, Ann Arbor, Michigan, USA, <sup>4</sup>International Center for Marine Studies, Shanghai Ocean University, Shanghai, China

**Abstract** Lake Superior, the largest lake in the world by surface area and third largest by volume, features strong spatiotemporal thermal variability due to its immense size and complex bathymetry. The objectives of this study are to document our recent modeling experiences on the simulation of the lake thermal structure and to explore underlying dynamic explanations of the observed modeling success. In this study, we use a three-dimensional hydrodynamic model (FVCOM—Finite Volume Community Ocean Model) and an assimilative weather forecasting model (WRF—Weather Research and Forecasting Model) to study the annual heating and cooling cycle of Lake Superior. Model experiments are carried out with meteorological forcing based on interpolation of surface weather observations, on WRF and on Climate Forecast System Reanalysis (CFSR) reanalysis data, respectively. Model performance is assessed through comparison with satellite products and in situ measurements. Accurate simulations of the lake thermal structure are achieved through (1) adapting the COARE algorithm in the hydrodynamic model to derive instantaneous estimates of latent/sensible heat fluxes and upward longwave radiation based on prognostic surface water temperature simulated within the model as opposed to precomputing them with an assumed surface water temperature; (2) estimating incoming solar radiation and downward longwave radiation based on meteorological measurements as opposed to meteorological model-based estimates; (3) using the weather forecasting model to provide high-resolution dynamically constrained wind fields as opposed to wind fields interpolated from station observations. Analysis reveals that the key to the modeling success is to resolve the lake-atmosphere interactions and apply appropriate representations of different meteorological forcing fields, based on the nature of their spatiotemporal variability. The close agreement between model simulation and observations also suggests that the 3-D hydrodynamic model can provide reliable spatiotemporal estimates of heat budgets over Lake Superior and similar systems. Although there have been previous studies which analyzed the impact of the spatiotemporal variability of overwater wind fields on lake circulation, we believe this is the first detailed analysis of the importance of spatiotemporal variability of heat flux components on hydrodynamic simulation of 3-D thermal structure in a lake.

### 1. Introduction

Bounded by Ontario and Minnesota to the north and west, and Wisconsin and Michigan to the south, Lake Superior is the largest freshwater lake in the world by surface area of  $\sim 82,100$  km<sup>2</sup> and the third-largest freshwater lake by volume of 12,100 km<sup>3</sup>. The average water depth in Lake Superior is 147 m, ranging from a few meters near the coast to  $\sim 200$  m in the shallower western basin, to roughly 250–400 m in the deeper central and eastern basins (Figure 1).

The thermal structure of Lake Superior is a key physical indicator of climate change as well as a critical influence on regional climate and the lake ecosystem. Changes in lake temperature are mainly caused by surface heat fluxes over the lake (positive and negative), which interactively depend on lake surface water temperature. In a study by *Austin and Colman* [2007], surface water temperature in Lake Superior was reported to be increasing at a faster rate (0.12°C/yr) than the surrounding air temperature through a positive feedback involving lake temperature, absorption of the surface heat flux and ice coverage [*Austin and Colman*, 2007]. In addition, large climate variability such as extremely cold water and high ice coverage on the Great Lakes has been frequently observed [*Wang et al.*, 2012; *Clites et al.*, 2014]. Strong “thermal inertia” is considered

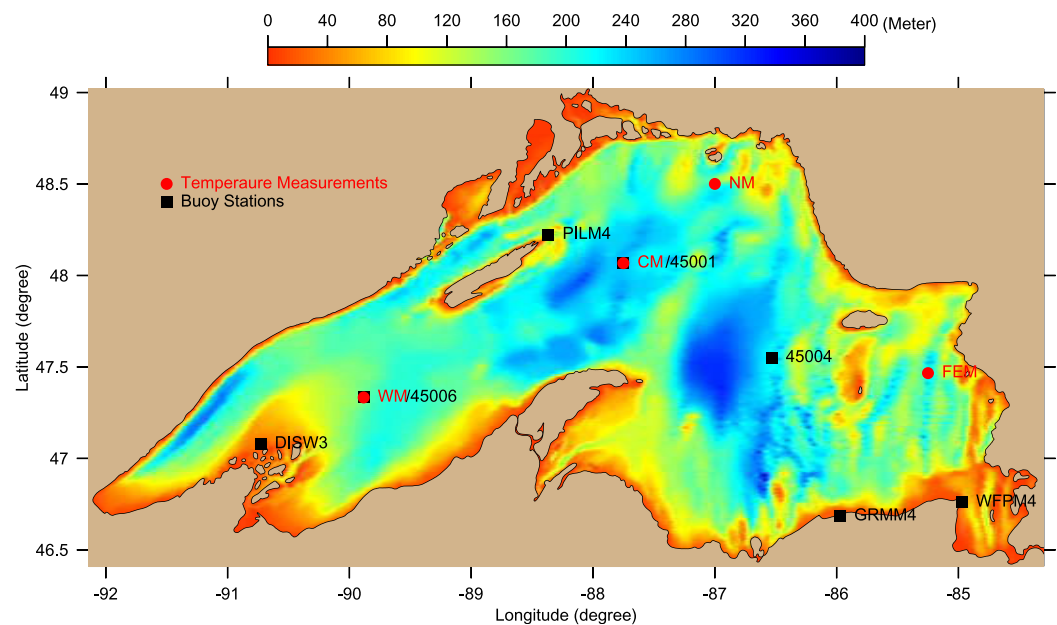


**Figure 1.** Bathymetry of Lake Superior. Water temperature measurements and meteorological buoy stations are denoted by red dots and filled squares, respectively.

one of the major reasons for the important leads and lags between water temperature, evaporation and ice coverage in the coupled lake-atmosphere system [Spence *et al.*, 2013; Lenters *et al.*, 2013]. At the lake-scale, the thermal gradients in Lake Superior influence vertical stratification and mixing, and contribute to the formation, evolution, and intensification of coastal currents [Schwab *et al.*, 1995; Beletsky *et al.*, 1999; Chen *et al.*, 2001; Rao and Schwab, 2007; Bennington *et al.*, 2010], providing direct and indirect impacts on the ecosystem such as nutrient availability, plankton abundance, and larval fish dispersal.

As the largest of the five Laurentian Great Lakes, Lake Superior is characterized by immense surface area, large water depth, and complex bathymetry. Consequently, the thermal structure of Lake Superior exhibits large spatiotemporal variability. The lake-averaged surface temperature varies seasonally between 0 and  $\sim 20^{\circ}\text{C}$  and its spatial temperature difference may exceed  $0.01^{\circ}\text{C}/\text{m}$  in the thermal front region. Due to its large surface area and water depth, the interannual variability of the surface water temperature of Lake Superior may exceed  $\pm 30\text{--}40\%$  relative to its climatological mean during the summer time, which is the largest interannual variability of all five Great Lakes (Figure 2). The time of the onset of stratification, the time of fall overturn, and the magnitude of thermal stratification vary significantly depending on the geographic location and meteorological conditions. Lake Superior's coast is less densely populated and has a relatively sparse observational sampling network compared to the other Great Lakes, adding more difficulties in accurate estimation of the three-dimensional lake thermal variability. It is therefore a major challenge to evaluate and predict the thermal structure at both local and basinwide scales.

The thermal structure and its variability in Lake Superior are closely linked to the interactions between surface heat fluxes, wind fields, and hydrodynamics of the system. Austin and Allen [2011] used a one-dimensional model to demonstrate to first-order sensitivity of summer surface water temperature, heat content, and vertical stratification scale to air temperature, wind speed, and the previous winter's ice cover. Due to very limited observations, previous estimates of surface heat flux yielded mixed results, suggesting large uncertainties in estimation of the surface heat fluxes in Lake Superior [Schertzer, 1978; Lofgren and Zhu, 2000]. More recent observations [Blanken *et al.*, 2011; Spence *et al.*, 2011] show that the largest latent and sensible heat losses from the lake typically occurred in 2–3 day-long events, controlled by the surface wind patterns, the lake/air temperature difference, and humidity. These events account for significant heat release from the lake, accounting for the majority of the latent heat loss (70–88%) and sensible heat loss (97–99%) [Blanken *et al.*, 2011]. These findings suggest that the interactions of surface heat fluxes and lake thermal structure must be resolved at sufficiently high temporal and spatial resolution in hydrodynamic modeling for accurate simulation of thermal variability of Lake Superior. Wind also plays a critical role in determining the thermal structure

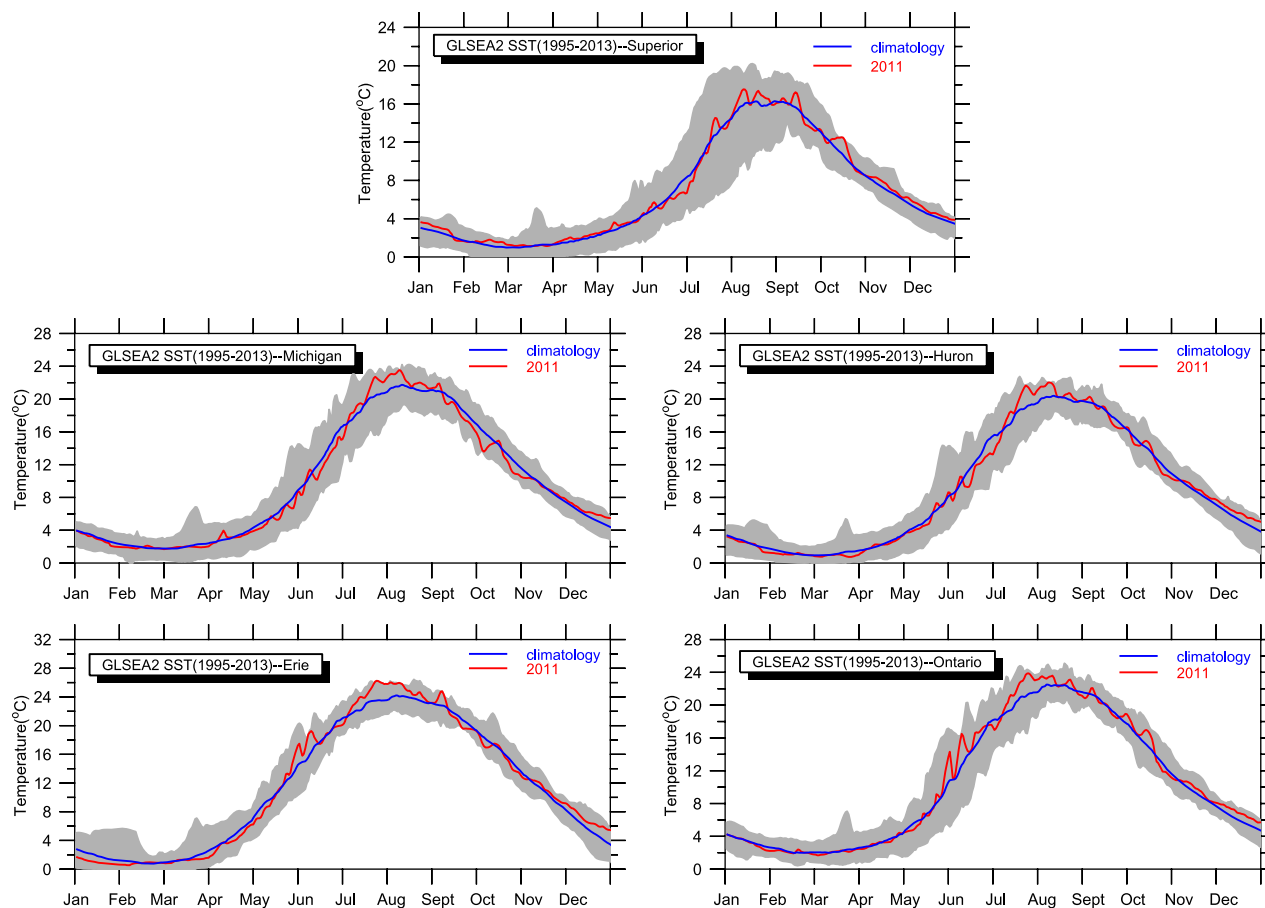


**Figure 2.** Time series of daily lake-averaged surface water temperature over the period 1995–2013, derived from GLSEA2. (<http://coastwatch.glerl.noaa.gov/>). Gray shadow areas indicate the interannual variability.

by influencing circulation, mixing processes, and latent and sensible heat fluxes. Recent work by *Beletsky et al.* [2013] demonstrated the potential shortcomings of interpolated wind conditions over Lake Erie in accurately representing circulation and thermal structure. *Huang et al.* [2010] studied the sensitivity of model results to meteorological forcing for Lake Ontario, showing that the difference between simulations using observed and meteorological model forcing are mainly due to the difference in wind stress in their experiments and can cause significant changes of water temperature in the thermocline. *Chen et al.* [2004] used QuikSCAT winds for atmospheric forcing and compared the simulation driven by wind field interpolated from moored buoys and land-based meteorological stations. The results show that the wind field constructed from either observation by interpolation or QuikSCAT was not sufficient to provide a reliable and accurate simulation of coastal currents and stratification in Lake Superior, and leaves open the question of how to accurately represent the mesoscale wind variability over Lake Superior.

Numerical modeling is one of the most valuable tools to understand the complexity of natural water systems and has been applied to Lake Superior with various focuses. The hydrodynamic modeling of Lake Superior began with a simplified diagnostic model to simulate the lake-wide currents, in which lake temperature and meteorological forcing were prescribed [Lam, 1978]. *Chen et al.* [2001] developed a three-dimensional, prognostic hydrodynamic model for Lake Superior using a nonorthogonal coordinate transformation, primitive equation, and coastal ocean circulation model. This model was used for a process-oriented study on the formation and evolution of the Keweenaw current associated with local wind and thermal gradients [Zhu et al., 2001; Chen et al., 2004]. Recently, long-term simulations were conducted to investigate the large-scale circulation pattern in Lake Superior with a focus on the climatological state and interannual variability [Bennington et al., 2010; Bai et al., 2013] and to examine the lake biophysical processes [White et al., 2012]. Dupont et al. [2012] configured and assessed a NEMO (Nucleus for European Modelling of the Ocean)-based hydrodynamic modeling system for the Great Lakes, with a focus on Lake

Ontario. However, there have been no studies showing comprehensive examinations on modeling performance in simulating the thermal structure of Lake Superior and none of the studies examined the relationship between the representation of the lake-atmosphere system in a model and the model performance in simulating the thermal structure from the perspective of modeling dynamics per se, hence the following questions remains unaddressed: (1) How do lake-atmosphere interactions impact the variability of the lake thermal structure? (2) How do the specific representations of meteorological forcing affect the simulation accuracy of the lake thermal structure? (3) What is the optimal configuration for a hydrodynamic modeling system of Lake Superior based on the existing observation resources?

Since 2002, Lake Superior has been part of the National Oceanic and Atmospheric Administration's (NOAA) operational Great Lakes Coastal Forecasting System (GLCFS). The GLCFS runs a version of the Princeton Ocean Model for each of the Great Lakes several times per day using observed surface meteorology for nowcasting and NOAA weather forecasts for predicting lake hydrodynamics up to 5 days in advance [Schwab and Bedford, 1994]. Since its inception, GLCFS has used a surface heat flux submodel which dynamically calculates the sensible, latent, and upward longwave heat fluxes within the hydrodynamic model, using the surface water temperature from the hydrodynamic calculation, as opposed to precomputing heat flux based on an assumed water temperature [Schwab and Bedford, 1994]. This strategy was adopted early in the development of GLCFS and seemed to provide more accurate temperature simulations, although this hypothesis was not rigorously tested.

On the other hand, hydrodynamic modeling with prescribed (forced) surface heat fluxes is not unusual and has been adopted in previous studies using a variety of community models (e.g., (Princeton Ocean Model) POM, Regional Ocean Modeling System (ROMS), and FVCOM). Such practices have also been widely used in various hydrodynamic simulations in oceans and large lakes [Chen *et al.*, 2001; Beletsky *et al.*, 2006; Roed and Albrechtsen, 2007; Haidvogel *et al.*, 2008; Huang *et al.*, 2010; Mason *et al.*, 2011; Beardsley *et al.*, 2013]. Prescribed surface heat fluxes are commonly obtained from reanalysis data sets, meteorological models, or local observations. Although its simplicity is attractive, a major drawback of using precomputed surface heat flux is the potential for inadequate resolution of complex air-sea interactions. Because of this, artificial flux adjustments or temperature restoration might be required in the model simulations [Marchesiello *et al.*, 2003; Penven *et al.*, 2005; Haidvogel *et al.*, 2008; Xu and Malanotte-Rizzoli, 2013].

In other regions, recent studies demonstrated the critical role of resolving air-sea interactions in improving the simulation of sea surface temperature [Wei *et al.*, 2013; Xue *et al.*, 2014] and the underlying mechanisms vary significantly depending on characteristics of the regional climate. For the Great Lakes region, there have been no studies examining such matters and their influence on model performance. The primary goals of this paper are (1) to apply FVCOM to simulate the thermal structure of Lake Superior, (2) to quantitatively assess the impact of using dynamically computed heat flux in Lake Superior (and, by inference, other Great Lakes and similar coastal regions), (3) to compare the results obtained by using three different types of meteorological forcing (one based on interpolation of surface weather observations, on WRF, and on CFSR reanalysis data), and (4) to identify the primary factors which impact model accuracy and investigate the underlying dynamics. Although there have been previous studies which analyzed the impact of the spatiotemporal variability of overwater wind fields on lake circulation, we believe this is the first detailed analysis of the importance of spatiotemporal variability of heat flux components on hydrodynamic simulation of 3-D thermal structure in a lake.

The remaining sections of this paper are organized as follows. In section 2, the data, the models, and the design of the numerical experiments are described. In section 3, the spatiotemporal variability of the lake thermal structure is examined based on observed and simulated results, and modeling advances in simulating the lake thermal structure are presented in detail. A discussion of the results is presented in section 4, and the conclusions are summarized in section 5.

## 2. Data, Models and Experimental Design

### 2.1. Data

To characterize the lake thermal structure, we compiled both satellite imaginary and in situ hydrographic data with an aim to capture large spatial variability of the thermal structure in Lake Superior. The Great Lakes Surface Environmental Analysis (GLSEA2) provides comprehensive information on lake surface water temperature, which is derived from NOAA/AVHRR (Advanced Very High-Resolution Radiometer) satellite

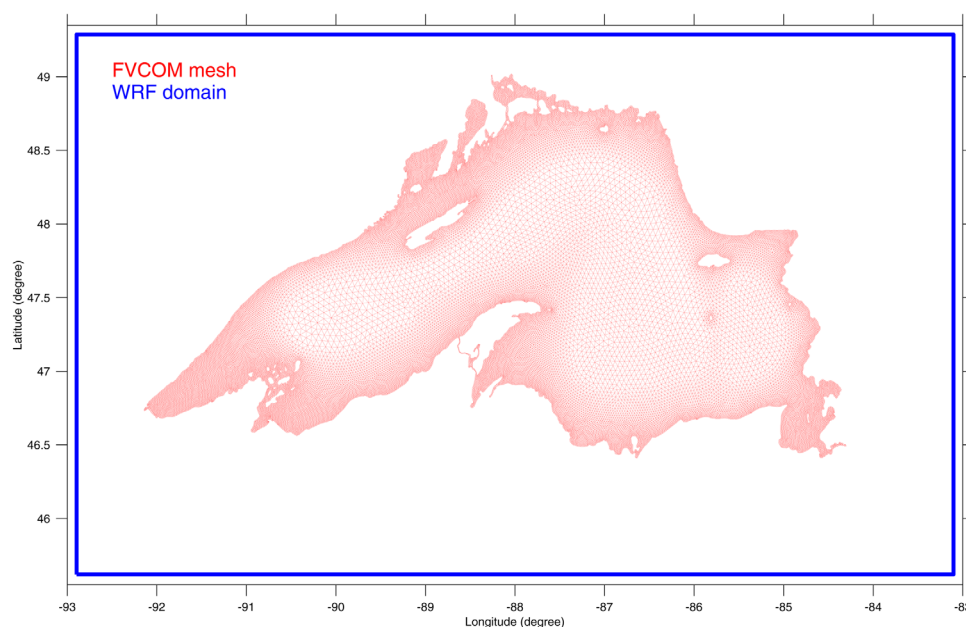


**Figure 3.** FVCOM model mesh with unstructured triangular grids. The box denotes the WRF model domain.

imagery. GLSEA2 are updated daily with information from the cloud-free portions of the satellite imagery. A smoothing algorithm is applied to the map for days when no imagery available [Schwab *et al.*, 1992]. GLSEA2 data cover the period from 1992-present and serve as the best resource to examine the spatial and temporal variability of the surface water temperature. We noted here the GLSEA2 is a product based on ice-free observations (e.g., open water) only. Figure 2 presents interannual and seasonal variabilities of lake-averaged surface water temperature derived from the GLSEA2 data. As the surface water temperature in 2011 closely follows the climatological mean (Figure 2), we chose year 2011 as a “typical” year for modeling experiments. Recently, significant achievements have been made in deploying hydrographic measurements in Lake Superior [Austin, 2013]. Four moorings deployed by University of Minnesota-Duluth in the Western, Central, and Northern and far Eastern sites for the year 2011 are also used to validate the water temperature vertical profiles. Meteorological observations including air temperature, dew point, wind direction, wind speed, cloud cover, barometric pressure, and surface water temperature over Lake Superior are collected from National Data Buoy Center (NDBC) and used to derive meteorological forcing for the hydrodynamic model and used for wind assimilation in the meteorological model. Meanwhile, a separate set of meteorological forcing for the hydrodynamic model is also retrieved from the CFSR at hourly temporal resolution and 20 km horizontal resolution from the gridded reanalysis data [Saha *et al.*, 2014] (Note that data resolution has been increased from the original 0.3° resolution in CFSR to approximately 0.2° since 2011).

## 2.2. Models

The hydrodynamic model used in this study is FVCOM (Finite Volume Community Ocean Model) [Chen *et al.*, 2006]. FVCOM is an unstructured-grid, finite-volume, three-dimensional (3-D), primitive equation ocean model with a generalized terrain-following coordinate system in the vertical and nonoverlapping triangular meshes in the horizontal. With the merit of an unstructured grid providing ideal geometrical fitting and flexibility of local topography refinement, FVCOM has gained popularity in research and applications to estuaries, coastal oceans, and the Great Lakes [Xue *et al.*, 2009; Shore, 2009; Zhao *et al.*, 2010; Anderson and Schwab, 2013; Bai *et al.*, 2013; Beardsley *et al.*, 2013]. There are other coastal hydrodynamic models [e.g., Beletsky *et al.*, 2006; Fujisaki *et al.*, 2013; Dupont *et al.*, 2012; White *et al.*, 2012 and many others.] with similar characteristics to FVCOM, but we chose the FVCOM model because it is currently being used by NOAA for operational forecasting in several coastal regions and is scheduled to replace the Princeton Ocean Model in NOAA's GLCFS. The Lake Superior FVCOM model is configured with a horizontal resolution of <100 m around the islands and waterways, 200–300 m along the coast and the bathymetric slope, and ~2 km in the central and eastern basin (Figure 3), with a total of ~120,000 model elements for each vertical layer.

**Table 1.** The Configuration of Numerical Experiments

Experiments	Sensible/Latent/Upward Radiation Flux	Solar Radiation/Downward Longwave Radiation Flux	Wind
C1-I	Precomputed	Observation-interpolated	
C1-II	Precomputed	WRF-simulated	
C1-III	Precomputed	CFSR	
C2-I	Dynamically calculated	Observation-interpolated	
C2-II	Dynamically calculated	WRF-simulated	
C2-III	Dynamically calculated	CFSR	
Hybrid Forcing	Dynamically calculated	Observation-interpolated	WRF-simulated

The Lake Superior-FVCOM model contains 40 vertical sigma coordinate layers with a vertical resolution of < 1 m in the coastal region and 5–10 m in the open basin. The high-resolution (in both the horizontal and vertical) model is designed to accurately resolve the cross-shore scale of thermal fronts and coastal currents, and capture the dynamics of the surface and bottom boundary layers in the regions with steep topographic gradients as key requirements to resolve multiscale processes in Lake Superior as a part of our long-term modeling development goal.

The 3.1.1 version of WRF is used in this study to simulate the meteorological conditions over Lake Superior. The WRF domain (Figure 3) has a geographic extent of 81.2°W–83.5°W and 41.6°N–43.5°N with a horizontal resolution of 8 km, which results in 80×50 grid points using a Lambert map projection. Twenty-seven vertical levels were specified with finer vertical resolution in the surface boundary layer. Lake Superior-WRF is initialized using the National Centers for Environmental Prediction Final (NCEP FNL) operational global analysis data on 1° by 1° grids prepared operationally every 6 h for lateral boundary condition. The high-resolution, daily Real-Time, Global Sea Surface Temperature (RTG\_SST) analysis with horizontal resolution of 0.083° (9–10 km) was used as the model lower surface boundary conditions over Lake Superior. The model was reinitialized every 2 days and run forward in time for 3 days. The first day of each run was discarded and the model results for days 2 and 3 were output and concatenated to produce continuous forcing fields. The inclusion of observational data assimilation is a major advantage in the WRF model to constrain the model for more accurate simulation and forecasting. Six buoys from NDBC are selected for wind assimilation including stations 45001, 45004, 45006, DISW3, PILM4, and WFPM4 (Figure 1). The nudging method followed *Chen et al.* [2005] and a very weak assimilation impact with a nudging coefficient of 0.01 was applied to ensure the assimilation would not cause discontinuity of the atmospheric dynamics for the wind field. The horizontal and temporal resolution of the WRF model forcing are not adequate to resolve fast-moving, short wavelength atmospheric phenomena such as squall lines, so the impact of these relatively rare events on large-scale thermal structure and circulation, while assumed to be small, is not considered here. Nevertheless, in atmospheric models such as WRF, phase differences (e.g., timing of events), and spatial structure can have a considerable influence on short-scale processes such as storm-surge, water levels, and wind waves.

**2.3. Design of Experiments**

A series of numerical experiments were designed to examine the impacts of different atmospheric forcing configurations in the model (Table 1): Three types of surface forcing (I: Observation-interpolated, II: WRF-simulated and III: CFSR reanalysis data) are tested. The hydrodynamic model is driven by each forcing with two approaches (Categories). In category 1 (C1), the model is driven by precomputed (forced) surface heat flux. In category 2 (C2), we used an approach that dynamically calculates the surface heat flux based on the prognostic surface water temperature computed within the model as opposed to precomputing the heat flux based on the prescribed surface water temperature.

In case C1-I, the surface heat fluxes are derived from surface water temperature and meteorological conditions estimated from NDBC buoys, in which sensible and latent heat fluxes were calculated by the bulk transfer equations. Longwave and shortwave radiations were computed using the formulas from *Parkinson and Washington* [1979]; *Wyrki* [1965]; *Ivanoff* [1977]; *Guttman and Matthews* [1979]; and *Cotton* [1979]. The spatial interpolation of the observed wind and estimated surface heat flux is computed using the “natural neighbor” technique of *Sambridge et al.* [1995] (hereafter referred to as “observation-interpolated” wind and heat flux). In case C2-I, the surface wind, downward longwave radiation and solar radiation fields are the

same as used in case C1-I (i.e., “observation-interpolated”), while the instantaneous latent heat, sensible heat, and upward longwave radiation are calculated using the COARE algorithm by *Fairall et al.* [1996] within FVCOM based on simulated surface water temperature.

In case C1-II, surfacing heat fluxes and wind are precomputed by the WRF simulation with the model configuration described in previous section 2.2 (hereafter referred to as “WRF-simulated” wind and heat flux). In case C2-II, the surface wind, downward longwave radiation, and solar radiation are the same as used in case C1-II (“WRF-simulated”) and similarly, the latent heat, sensible heat, and upward longwave radiation are calculated dynamically using COARE algorithm within FVCOM. In case C1-III, the surface heat fluxes and wind are directly extracted from CFSR reanalysis data. In case C2-III, the surface wind and downward radiation are the same as that in case C1-III, and the latent heat, sensible heat, and upward longwave radiation are calculated dynamically within FVCOM. In addition, an experiment driven by a hybrid atmospheric forcing with “Observation-interpolated” solar and downward longwave radiation fields along with “WRF-simulated” wind fields was also conducted. A summary of the configuration of these experiments is presented in Table 1. All experiments are initialized in March with a homogeneous water temperature of 2°C and allow for a 1 month dynamic adjustment (model spin-up). Model results from April–December are used for the analyses.

### 3. Results: Observed and Simulated

#### 3.1. Climatology: Seasonal Cycle, Spatial Patterns, and Interannual Variability

In Lake Superior, the surface water temperature usually reaches its minimum during February and March with a warming trend until August (occasionally July or September) when the surface water reaches its highest temperature, and then starts to cool down in the autumn to form a seasonal cycle (Figure 2). In recognition of the seasonal pattern of surface water temperature, the hydrodynamic winter, spring, summer, and fall seasons in this paper are defined, respectively, as January–March (coldest water with ice coverage), April–June, July–September (warmest water), and October–December.

Due to the immense surface size and abruptly changing bathymetry, the surface water temperature in Lake Superior varies significantly, particularly during the summertime. Figure 4 shows the observed spatial pattern of the seasonal climatology of the surface water temperature (left) and its climatological variability indicated by the standard deviation relative to the climatological monthly mean (right), derived from GLSEA2 data (1995–2013). During the springtime (Figures 4a and 4b), the lake-wide surface temperature is spatially uniform with a mean temperature between 3 and 4°C except in the southern coastal region where warmer waters may reach 2–3°C higher. The temperature pattern reflects signatures of latitude variation and the local water depth, which are the primary driving factor for spring early warming in the southern coastal region. The temperature in the coastal region shows a relatively large interannual variability with a standard deviation of 1.2–1.6°C while smaller variability is observed in the open water (midlake) with the standard deviation of 1°C. This indicates that the timing of early spring coastal warming varies significantly each year, while lower temperature in the open water is observed with less interannual variability during the springtime.

In summer, the surface water temperature shows large spatiotemporal variability (Figures 4c and 4d). Along the southern coasts of the shallow western basin, the mean surface water temperature can reach ~18°C near the southern coastal region (e.g., near the Apostle Islands) while the 5–6°C colder water exists along the northern coast of the western basin, in part, due to the upwelling-favored winds. The coldest water (12–13°C) occupies the deep central and northern basins, with a cold core centered in the region near 87°W and 48°N. The strong cross-shore temperature gradients are known to play a significant role in maintaining and intensifying the baroclinic component of the coastal currents [*Beletsky et al.*, 1999]. The large climatological variability of surface water temperature during the summertime is illustrated in Figure 4D by a standard deviation of 2.5–3°C in the open water, which shows a strong signature of the local bathymetry (Figure 1). This is because more rapid heating in shallow water generates strong horizontal temperature gradients perpendicular to the shoreline and the warmer nearshore water moves gradually toward the lake center as the lake begins to stratify. Unlike the coastal waters, stratification may or may not develop in the central basin since more heating is required for a deeper water column to be stratified as well as the fact that surface wind mixing can dominate in the open water. Because of this, the central basin is occupied by cold unstratified

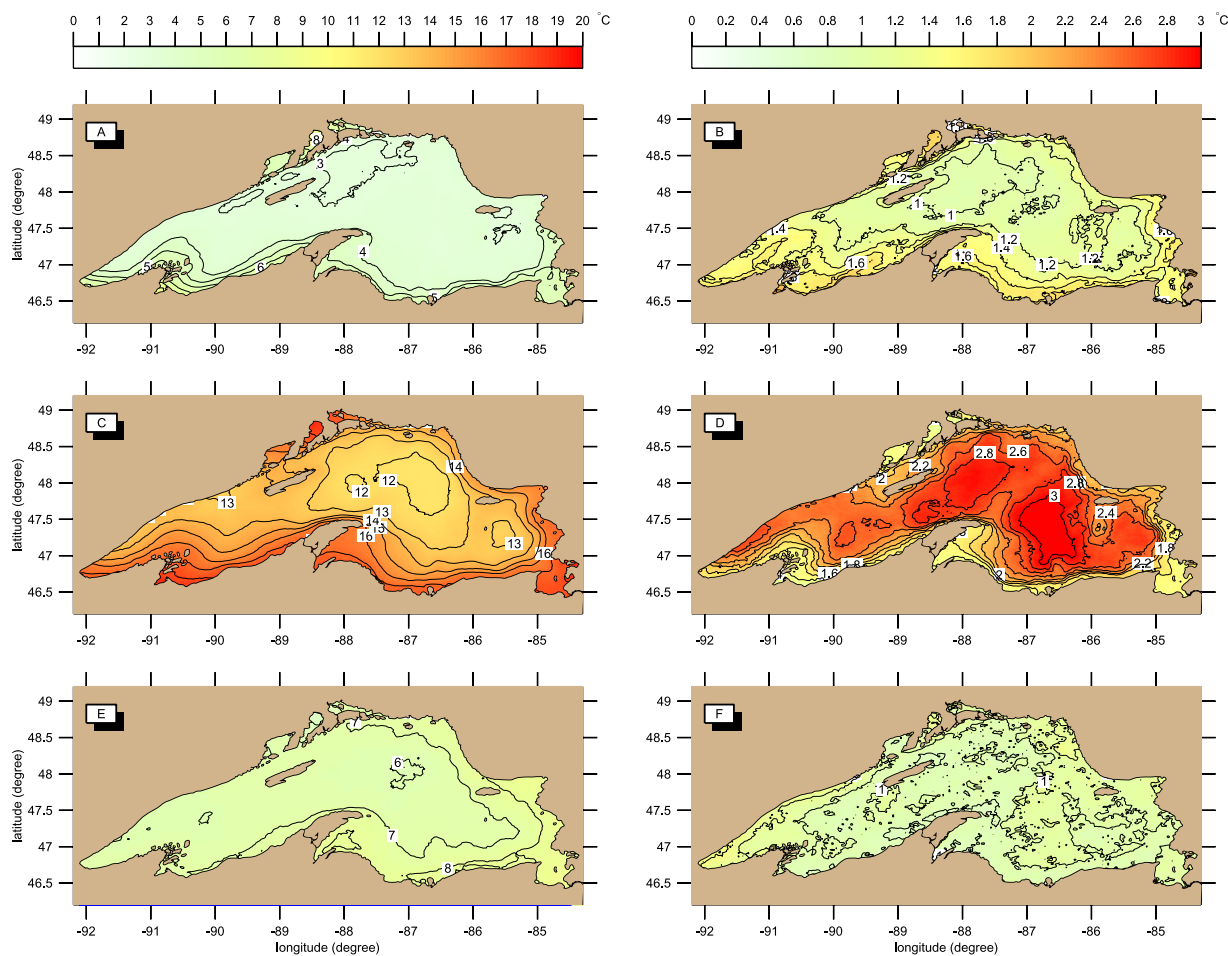


**Figure 4.** The horizontal distribution of the seasonal surface water temperature (left) and its standard deviation (right) relative to the climatological mean during ice-free seasons (spring: top, summer: middle and fall: bottom), derived from GLSEA2 data.

surface water or a warm upper layer from year to year. The large climatological variability during the summer is also clearly shown by the shaded envelop in Figure 2.

The lake surface temperature decreases from  $> 10^{\circ}\text{C}$  (October) to  $6^{\circ}\text{C}$  (December) during the fall, due to reductions in net radiation and increases in latent and sensible heat flux [Blanken *et al.*, 2011], often associated with stronger wind speeds with monthly mean  $\sim 6\text{--}7$  m/s (wind statistics were extracted from NDBC). The spatial pattern of surface water temperature is fairly homogenous with a mean value of  $\sim 6^{\circ}\text{C}$  and only the southern and eastern coastal regions may have slightly warmer water of  $7\text{--}8^{\circ}\text{C}$ . The interannual variability during the autumn is also significantly reduced with a standard deviation of  $1^{\circ}\text{C}$  (Figures 4e and 4f). Surface cooling continues through winter accompanied by rapid ice formation in the nearshore regions and relatively lower ice coverage in the open water (not shown), partly due to the strong wind that can retard midlake ice formation [Assel, 1990].

### 3.2. Model-Data Comparison

Figure 5 (and Table 2) presents the lake-average surface water temperature for 2011 (a “typical year,” see Figure 2), estimated from the six numerical experiments in categories 1 and 2 (Table 1, C1 and C2) in comparison to GLSEA2 daily data. The simulation with precomputed (forced) heat fluxes derived from observation-interpolated radiation and wind fields (case C1-l) clearly fails to capture the seasonal variability of the surface water temperature. In contrast, the model-simulated lake-averaged surface water temperature in case C2-l shows very good agreement with the GLSEA2 data (RMSE  $1.24^{\circ}\text{C}$ ). The model simulation accurately reproduces the seasonal cycles and also captures cooling and warming events that frequently

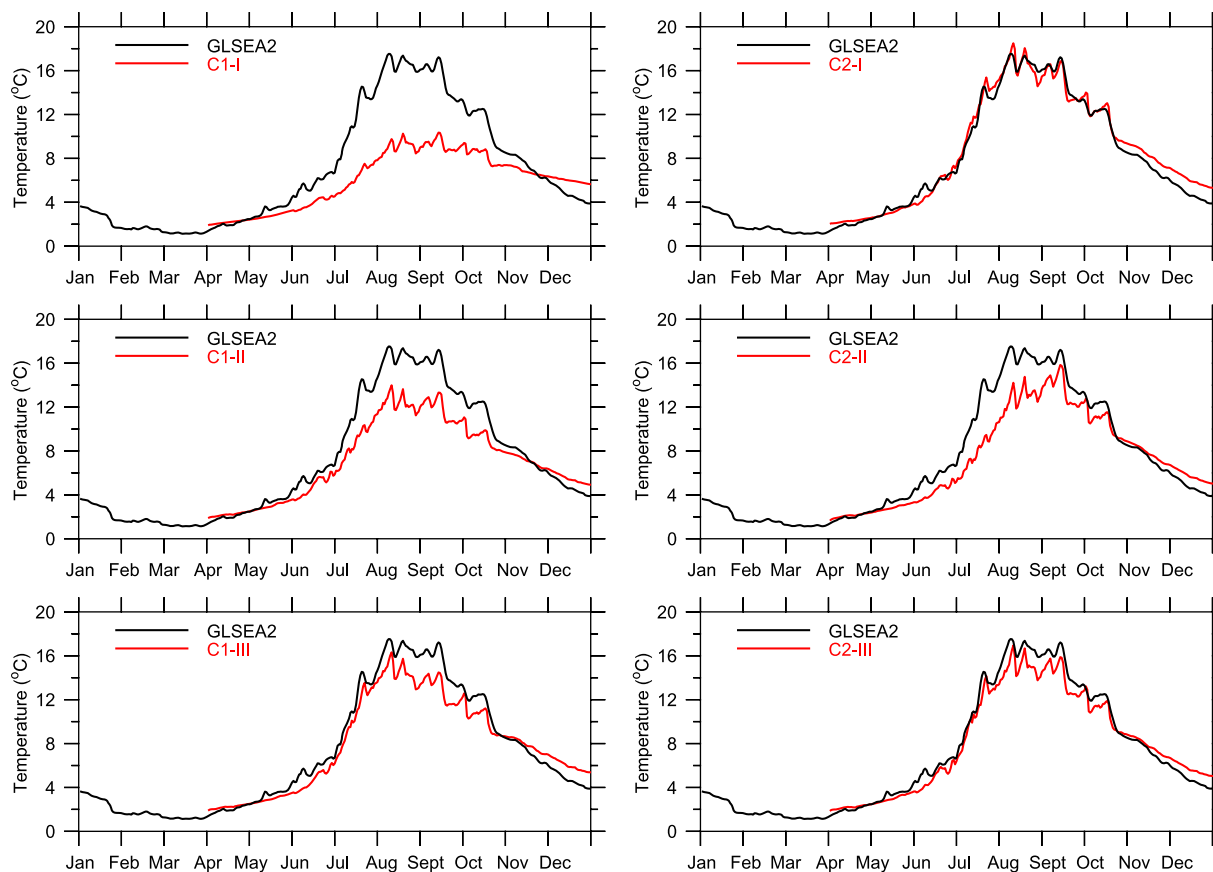


Figure 5. Time series of the lake-average surface water temperature simulated (red) in comparison to the GLSEA data (black) for year 2011 during the ice-free seasons.

occur during the summer and fall seasons on synoptic time scales, suggesting that the model adequately captures physical processes on different scales.

The simulated surface water temperature average in case C1-II with precomputed surface forcing by the WRF model shows better results compared to the case C1-I. However, the model results still drift away from GLSEA2 after July, and the model significantly underestimated the surface water temperature during the summertime by up to 4°C. In case C2-II, the simulation shows improvements compared to C1-II after August, with ~2–3°C warmer temperature in the late summer and fall seasons. The average RMSE is 1.19°C.

Table 2. The Spatial Root-Mean-Square-Error (RMSE (°C)-row 1, 4, 7,10), the Average Bias of Surface Temperature (Bias (°C)-row 2, 5, 8, 11) and the Spatial Correlation Coefficient (scc row-3, 6, 9, 12) of the Model Simulation in Comparison to GLSEA2<sup>a</sup>

	RMSE (°C)						
	Bias (°C)						
scc	C1-I	C1-II	C1-III	C2-I	C2-II	C2-III	Hybrid Forcing
Spring	0.85	1.32	0.94	1.01	0.62	0.88	0.75
	-0.74	0.27	0.01	0.50	-0.17	0.20	0.35
Summer	0.52	0.88	0.63	0.84	0.91	0.87	0.88
	5.47	2.89	2.64	1.54	2.28	1.47	0.99
Fall	-6.2	-2.42	-1.38	0.48	-2.20	-0.64	-0.36
	0.46	0.87	0.51	0.73	0.94	0.79	0.89
Average	1.22	0.76	1.02	1.16	0.67	0.73	1.14
	-0.50	-0.14	0.60	1.04	0.53	0.53	1.05
Average	0.50	0.60	0.59	0.75	0.82	0.78	0.74
	2.51	1.66	1.53	1.24	1.19	1.03	0.96
	-2.48	-0.76	-0.25	0.67	-0.61	0.03	0.34
	0.49	0.78	0.58	0.78	0.88	0.82	0.83

<sup>a</sup>Model results are interpolated into 15241 GLSEA2 grids of 1 km resolution for comparison.

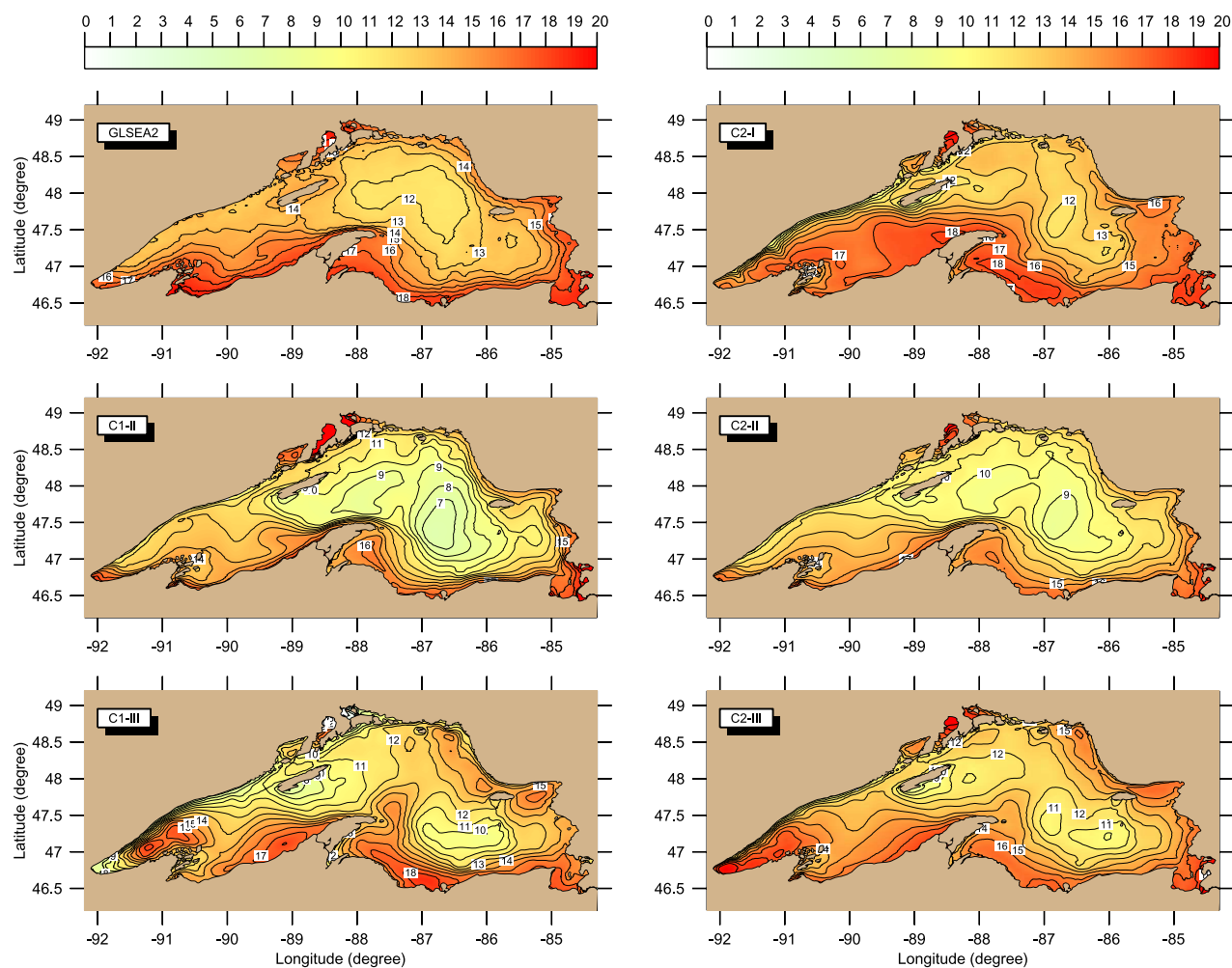


**Figure 6.** Horizontal distribution of the surface water temperature during the summer for year 2011 from GLSEA2 data and model simulations.

Again, from the comparison of the lake-wide average of surface water temperature, the simulation with CFSR forcing with the dynamically calculated heat flux (C2-III) shows a better result than the case with the CFSR precomputed heat fluxes (C1-III). C2-III shows significant improvements particularly in summer and early fall in comparison to the C1-III, which shows a 2–3°C cold bias after September and early October.

Lake Superior exhibits large spatial variability of surface water temperature (5–6°C) and strong thermal gradients during the summertime (Figure 6), so the assessment of lake-wide average of surface water temperature is only part of the picture. To fully understand the model results, a close comparison of the horizontal distribution of summer surface water temperature between GLSEA2 and the model results must be made. In Figure 6 and Table 2, results from case C1-II indeed show a spatial pattern of surface water temperature very similar to GLSEA2 ( $scc = 0.87$ ). The simulation reproduced the cold core in the central basin, the warmer water in the western basin, and strong thermal gradients near the southern coast, particularly near the northern Keweenaw coasts. Nonetheless, the simulation has an overall cold bias of ~ 2–4°C in the midlake, open water regions. Results from case C1-III with precomputed CFSR forcing provide smaller overall cold bias of lake temperature but show less correlated spatial pattern of SST ( $scc = 0.51$ ) to GLSEA2 in comparison with case C1-II.

When the sensible heat flux, latent heat flux, and upward longwave radiation are dynamically calculated through the COARE algorithm (C2-I, -II, -III), the simulation in case C2-I with “observation-interpolated” wind and downward radiative fluxes was able to eliminate the cold bias in terms of the lake-averaged surface water temperature (Figure 5). However, the simulated spatial pattern does not show very good agreement with the GLSEA2. Most regions in the western basin are overwarmed by 1–3°C and the cross-shore thermal

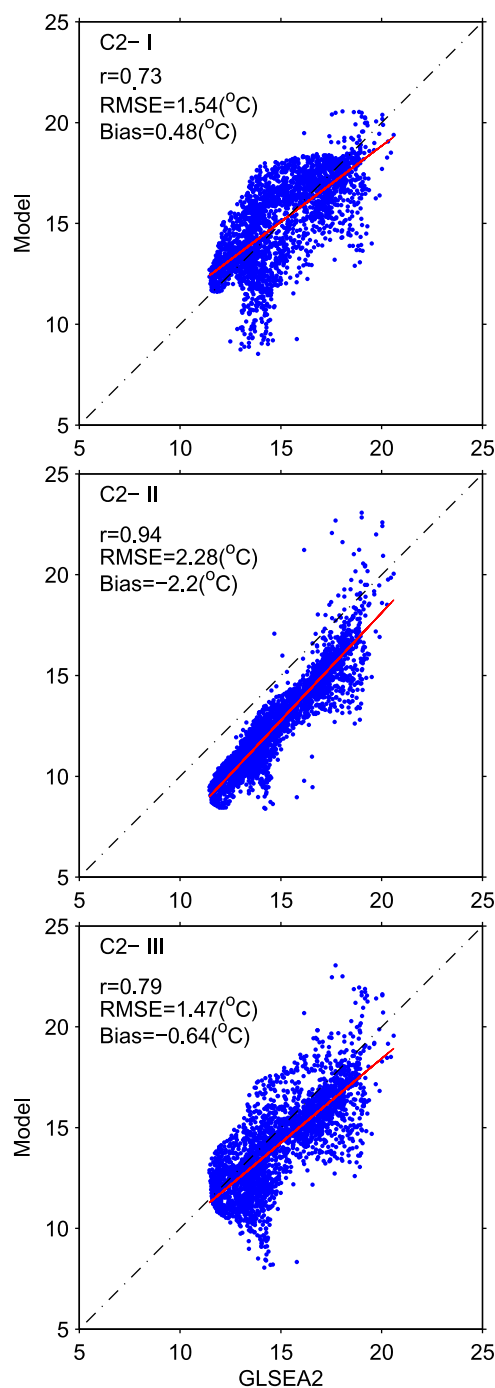


**Figure 7.** Scatter plots of model-computed surface water temperature via GLSEA2 data sampled at 5 km resolution for the case C2-I, C2-II, C2-III (see experiment design in section 2.3). Solid red lines indicate the best fit between model results and GLSEA2. Dashed lines are a diagonal line representing a perfect match. Correlation coefficients ( $r$ ) and RMS Error between model-computed and GLSEA2 values were estimated under  $p$ -value 0.05 (significance level).

the model also agrees well with the observation, at least below 10 m, (notice there are no observations in the upper 10 m at these two stations). In the northern basin, the model accurately reproduces the timing of summer stratification and the depth of the summer thermocline, with warm, surface water in the upper 20 m and cold water ( $\sim 4$ – $5^\circ\text{C}$ ) below 30 m. In the northern basin, the model appears to have overmixed

gradients near the southern coastal region are more diffusive than the GLSEA2. The thermal front near the northern Keweenaw coast is not well resolved compared to the GLSEA2 and the northern coastal region of the western basin appears to have too much thermal variability. On the other hand, the simulation in case C2-II with “WRF-simulated” wind and downward radiative fluxes shows a better spatial pattern compared to case C2-I. The simulation shows a highly correlated spatial pattern to GLSEA2. It also reduces the overall cold bias by  $2^\circ\text{C}$  compared to case C1-II. Despite these improvements, the result still shows an overall underestimation of surface water temperature by  $1$ – $2^\circ\text{C}$ . These comparisons are summarized by the one-on-one comparison of model simulation with GLSEA2 at 5 km gridded resolution for a clear visibility (Figure 7, top). Comparison shows the correlation coefficients between the model results and GLSEA2 are 0.73 (C2-I) and 0.94 (C2-II) and the RMSE are 1.54 and  $2.28^\circ\text{C}$ , respectively, evidenced by the more scattered points in case C2-I and less scattered but systematically shifted points in case C2-II. The C2-III results, on the other hand, show better agreement with smaller cold bias and a better spatial pattern of surface water temperature. In fact, C2-III is the best case among the six simulations with a relatively low RMSE of  $1.47^\circ\text{C}$  and high correlation coefficient of 0.79 (Figure 7, bottom).

Since the model in case C2-III provides, so far, the best simulation of temporal and spatial patterns of the surface water temperature, we further examined its performance in simulating the vertical structure of water temperature. Figure 8 shows the model-data comparison of the time evolution of the vertical thermal structure in the western, central, northern, and eastern basins. Overall the model results show close agreement with observations. In the shallower western basin, waters are stratified during early to mid-July (Figures 8a and 8b). Both model and observations show that the mixing depth is limited to a thin layer of 5–10 m near the surface during the summer and is completely mixed by late fall. In the deep central basin, the water stratifies in early August with much weaker vertical temperature gradients and colder surface water temperatures ( $12$ – $13^\circ\text{C}$ ) than that in the western basin. The surface mixed layer is deeper ( $\sim 15$ – $25$  m), with a thermocline varying between 15 and 30 m during summertime. The water begins to destratify by mid-September and the water column in the upper layer shows a temperature profile similar to that in the western basin through December. In the northern and eastern basins,

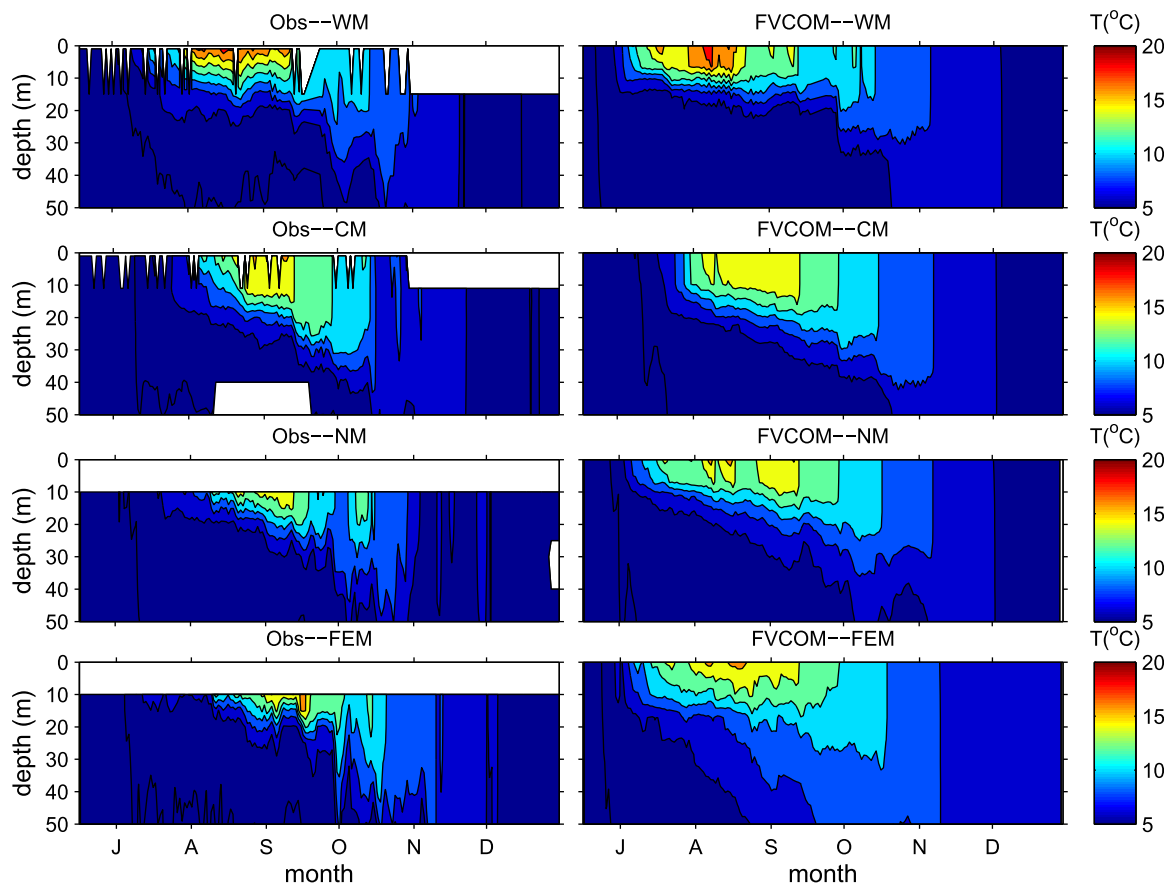


**Figure 8.** Mooring measured (left) and model-computed (right) temperature profile at upper 50 m at stations in the western basin (WM, total mooring depth 180 m), central basin (CM, total mooring depth 250 m), northern basin (NM, total mooring depth 195 m), and eastern basin (FEM, total mooring depth 250 m) (see Figure 1 for location).

the heat downward to the deeper waters during the summer and also slightly overestimated the autumn water temperature in the both stations in the northern and east basins.

The above results reveal that the model performance is very sensitive to the surface heat forcing. The simulation results with precomputed surface heat fluxes vary significantly depending on the data source, while the modeling with dynamically calculated heat fluxes persistently produces more reliable results. The RMSE, overall bias, and correlation to GLSEA2 (Table 2) for each season clearly show that model simulations in category 2 (driven by dynamically calculated surface heat fluxes) show significant improvements compared to the simulations in category 1 (driven by precomputed surface heat flux). Although dynamically calculated surface heat fluxes are already implemented in the GLCFS POM model, this is the first quantitative assessment of their impact on model accuracy. More specifically, the simulation with CFSR forcing (C2-III) produces overall the best simulation among the three experiments in category 2 while (1) the simulation with the “observation-interpolated” meteorological forcing produces the best lake-averaged surface water temperature and (2) the simulation with the “WRF-simulated” meteorological forcing produces more accurate spatial distribution of surface water temperature compared to the GLSEA2. We also note that (2) is consistent with the findings of *Beletsky et al.* [2013] for Lake Erie. A following question to ask is what are the primary mechanisms responsible for these observed model behaviors? Clearly, the underlying reasons for the model success must relate to using an accurate representation of the meteorological forcing fields and the associated dynamic interactions with lake surface temperature.

#### 4. Thermal Response of Lake Superior to the Meteorological Forcing

##### 4.1. Lake-Air Feedbacks

Recent studies show that SST simulation accuracy in coastal/regional ocean modeling can be significantly improved when local-scale negative feedback processes are resolved [*Seo et al.*, 2007; *Wei et al.*, 2013; *Xue*

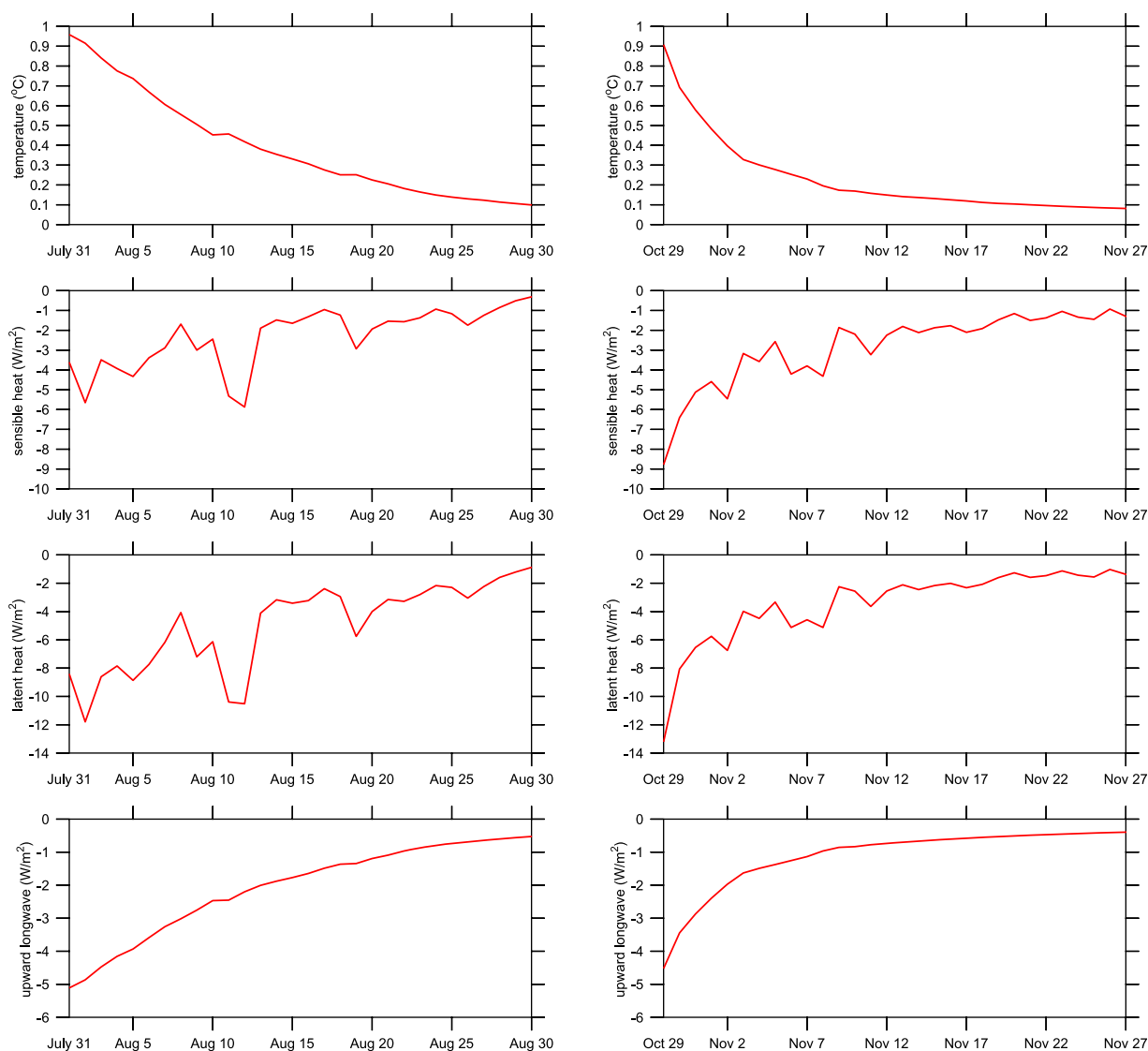


**Figure 9.** The restoration of the surface water temperature and corresponding adjustments of the sensible, latent heat, and upward longwave radiative fluxes after the initial perturbation of the surface water temperature during the summer and fall.

*et al.*, 2014]. We speculate this is also the case for Lake Superior when the flux is dynamically calculated based on prognostic surface water temperature. To identify the impact of local-scale lake-air feedback processes on the surface water temperature, we examine the model response to the perturbation of surface water temperature. In two process-oriented cases, a one-time perturbation of surface water temperature was imposed on 30 July (summer case) and 28 October (90 day later, fall case), respectively, in which the water temperatures in the upper 5 m were artificially increased by 1°C. By examining the responses of surface heat fluxes (and subsequent changes in water temperature) to the initial water temperature perturbation, we examine the feedback processes resolved in the model.

Figure 9 shows the changes in surface water temperature and surface heat fluxes after the initial perturbation. The results clearly show that the surface water temperature tends to revert back to the “reference state” of the normal simulation from its perturbation. The two cases revealed somewhat dissimilar dynamic adjustment of surface heat fluxes in response to the perturbation of the surface water temperature. Specifically, the restoration proceeded much faster in the autumn. It took about 5 days to remove 65% of perturbation impact on the surface water temperature in the autumn case while in the summer, there was still 45% of the perturbation impact remaining after 10 days. Accordingly, stronger adjustments of the surface heat flux were observed in the autumn case (Figure 9, middle) in addition to the impact of stronger mixing

that can cause the downward transfer of the perturbation-induced heat. The adjustment was particularly striking for sensible heat flux, which was roughly a factor of two larger in the autumn case, compared to summer (i.e., immediately after the perturbation was applied). Differences in latent heat flux were also apparent, but relatively lower (roughly a 30% increase in the autumn). Two strong wind events (1 August and 12 August) are also reflected in the temporal pattern of the surface heat flux adjustment (Figure 9).

Due to the faster restoration of surface water temperature in the autumn, the adjustments of the sensible and latent heat flux also attenuate faster in the autumn case. The adjustments of upward longwave radiation in the two perturbation cases are comparable in magnitude, and both are  $\sim 5 \text{ W/m}^2$  in the first day since it is controlled by the surface water temperature based on the Stefan-Boltzmann law. The faster restoration in the autumn case is also consistent with the fact that the latent and sensible heat fluxes are more significant during autumn. During this period, the turbulent heat fluxes are driven by the stronger wind and larger lake-air temperature and humidity gradients, which control the fluxes of latent heat ( $H_l$ ) and sensible heat ( $H_s$ ) according to the bulk formulae:

$$H_l = \rho_a L_e C_e U_{10} (q_s - q_a) \quad (1)$$

$$H_s = \rho_a C_p C_s U_{10} (T_s - T_a) \quad (2)$$

where  $\rho_a$  is the air density,  $L_e$  is the latent heat of vaporization,  $C_p$  is the specific heat capacity of air,  $C_e$  and  $C_s$  are the latent and sensible heat transfer coefficients,  $U_{10}$ ,  $T_a$ , and  $q_a$  are the wind speed, air temperature, and the specific humidity of air at the 10 m reference level above the sea surface, and  $T_s$  and  $q_s$  are surface water temperature and saturated specific humidity at the water surface.

These simple experiments demonstrate that the model with surface heat flux calculated dynamically is able to (partly) resolve the local lake-air feedback process as opposed to the model driven by forced surface heat fluxes, hence producing more accurate instantaneous surface heat fluxes based on the prognostic surface water temperature. These local negative feedbacks allow the surface heat flux to be resolved dynamically to keep the surface water temperature from drifting away from its equilibrium state. Furthermore, the temporal and spatial variability of surface heat flux that is calculated dynamically reflects the real-time lake-air feedback processes. Previous studies have shown that models can suffer systematic bias in SST simulation in regional seas (even though the mean state of surface heat flux was correctly specified) if the high-frequency variability of the surface heat flux does not match the response time scale of local air-sea feedbacks [Xue and Eltahir, 2015]. Although our model configuration is not able to fully resolve the lake-air interactions (e.g., the lake-air interactions in response to the perturbation of surface water temperature also affect the low-level cloud coverage and wind fields, which consequently affect the incoming solar radiation, and latent and sensible heat fluxes), the analyses help to explain the dynamical reasons why the model produces a better simulation when driven with dynamically computed surface heat fluxes than when driven by the precomputed surface heat flux.

#### 4.2. Impact of Wind

The “WRF-simulated” wind shows excellent agreement with the measured wind at the buoy stations. Figure 10 shows a comparison of the time series of the modeled and observed wind at four assimilated wind stations and one unassimilated wind station (for verification purpose). However, Experiments of C1-II and C2-II show that the spatial pattern of surface water temperature in the model simulation is much more coherent with the observed pattern when the model is driven by the “WRF-simulated” wind compared to the “observation-interpolated” wind. The mechanism through which wind affects the surface water temperature pattern is either through its impact on the surface currents (e.g., southwesterly or westerly winds may strengthen the cross-shore thermal gradients in southern coasts coast due to the Ekman Transport) and/or through its direct impact on sensible and latent heat fluxes (equations (1) and (2)), which is controlled by local wind speed.

Figure 11 presents a comparison of the seasonal-averaged wind fields overlaid with the mean value of hourly wind speed for each season over Lake Superior. The “observation-interpolated” wind, “WRF-simulated” wind, and CFSR wind agree with each other in the general pattern in terms of seasonal-averaged wind fields. In the spring, northeasterly wind dominates, except in the eastern basin where “observation-interpolated” produced somewhat stronger (indicated by the length of the arrows) mean

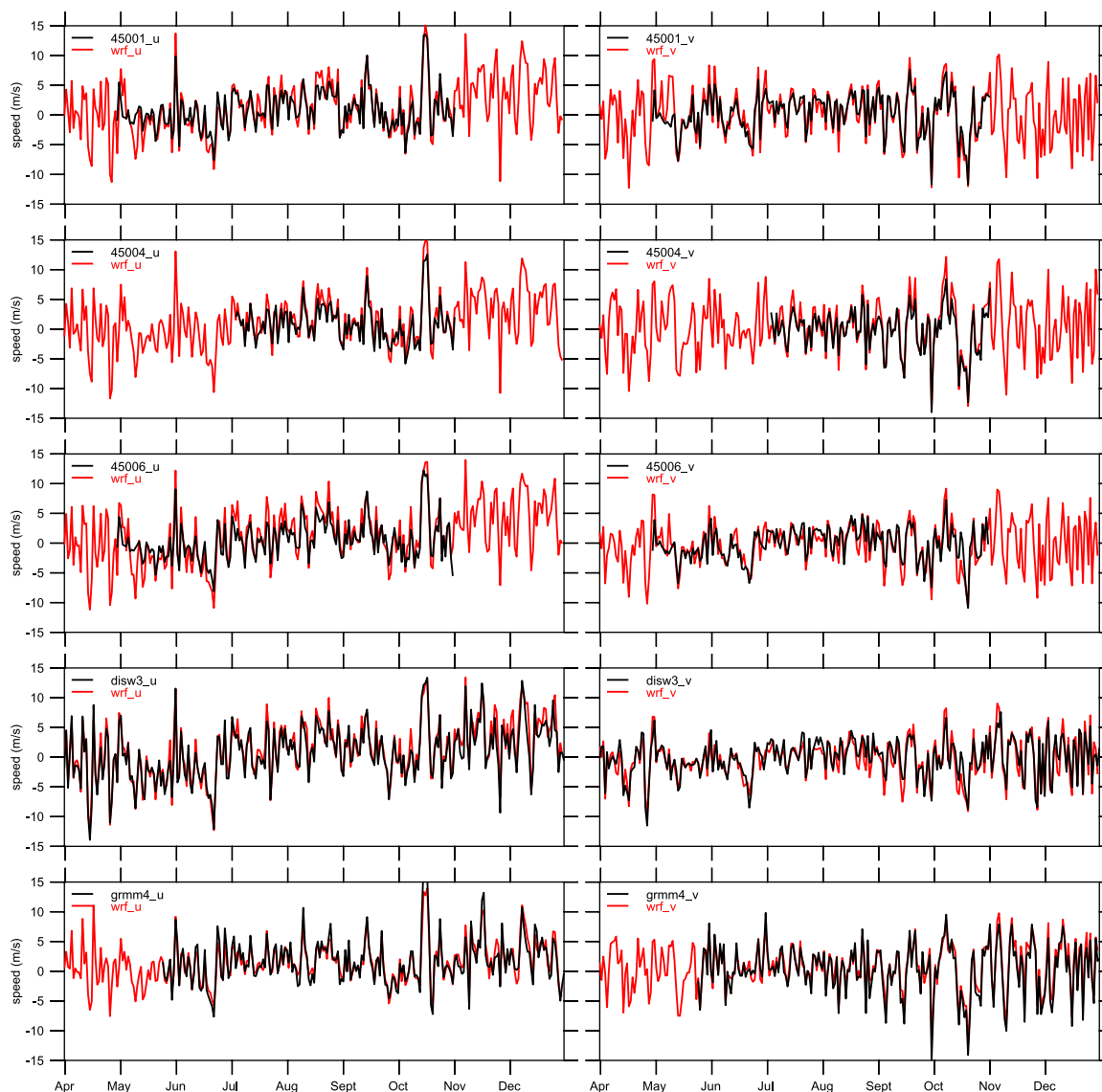


**Figure 10.** Time series of eastward (left) and northward (right) components of modeled (red) and observed (black) wind at four assimilated wind stations (top) and one unassimilated wind stations (bottom).

northeasterly wind field while the “WRF” and CFSR show weaker easterly wind. During the summertime, wind direction reverses and southwesterly wind prevails over the lake. During the autumn, wind becomes stronger and westerly wind prevails over the lake while local northwesterly wind prevails over the northern coast of the western basin.

However, the spatial patterns of wind speed (contours in Figure 11) show considerable difference between the “observation-interpolated” and the other two wind fields at finer spatial scales, especially in nearshore regions. The “WRF-simulated” wind and CFSR wind fields in all seasons show generally stronger winds over the open water in the midlake region, while the wind speed reduces quickly in coastal regions, showing strong cross-shore gradients. These important characteristics can impact the local sensible and latent heat fluxes and are not captured in the “observation-interpolated” wind, which most likely explains why the model with “WRF-simulated” and CFSR wind produces a better spatial pattern of the surface water temperature, particularly in the near shore region.

This suggests that differences in wind speed, rather than the wind direction, between the “observation-interpolated” wind and “WRF-simulated” or CFSR wind fields are much more significant in the hydrodynamic simulation, at least in terms of its impact on the simulation of spatial structure in the surface water

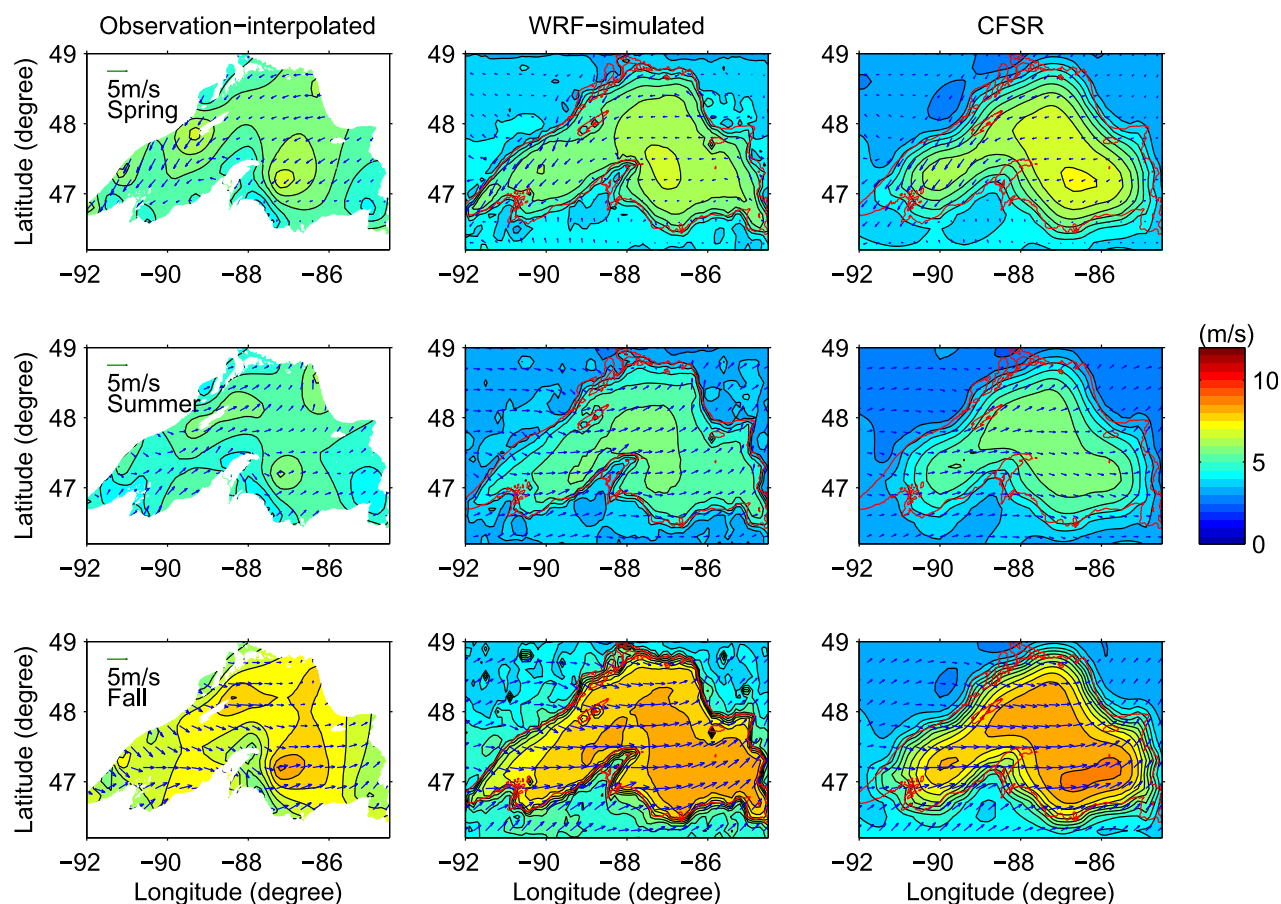


**Figure 11.** The “observation-interpolated” (left) and “WRF-simulated” (middle) and CFSR (right) seasonal-mean wind (arrow) overlaid with the mean value of hourly wind speed (contour) for each season over Lake Superior.

temperature. The “observation-interpolated” wind assumes that the local wind field can be represented by linear combinations of the wind information from the observed wind buoy stations, which was shown to be inaccurate as the wind speed over Lake Superior exhibits large mesoscale variability. On the other hand, the “WRF-simulated” and CFSR wind are dynamically constrained and able to better resolve local wind variability reflecting the atmospheric dynamics at the land-lake transition. This is also consistent with the finding from *Beletsky et al.* [2013].

#### 4.3. Spatial Variability of Surface Heat Flux

As shown in previous experiments (Figure 5 and 6), using “observation-interpolated” shortwave radiation and downward longwave radiation effectively eliminated the cold bias from surface water temperature simulation of case C2-II. This is due to a higher estimate of incoming shortwave radiation by  $\sim 15 \text{ W/m}^2$  in the “observation-interpolated” radiation fields ( $234\text{--}265 \text{ W/m}^2$ ) compared to the “WRF-simulated” ( $213\text{--}251 \text{ W/m}^2$ ) during May–August. During September–December, the shortwave radiative fluxes estimated by the two approaches are similar, while a major difference of  $28 \text{ W/m}^2$  exists between the “observation-interpolated” ( $279\text{--}340 \text{ W/m}^2$ ) and the “WRF-simulated” ( $245\text{--}317 \text{ W/m}^2$ ) estimations of downward longwave radiation (supporting information Figures S1 and S2). The radiation fields estimated by the CFSR data set are very similar to “observation-interpolated” estimates, which explains why the simulation with CFSR forcing was able to produce relatively good results of lake-wide average of surface water temperature (supporting information Figure S1 and Figure 12). The fact that the “observation-interpolated” estimation in the shortwave and downward longwave radiative fluxes can be reliable depends to large extent on the different spatial scales in the atmospheric and lake dynamics. The incoming solar radiation and longwave radiation do not exhibit large spatial gradients and the spatial pattern is not strongly dependent on surface water temperature (Figure 12). Thus the estimates derived from observations are relatively accurate even

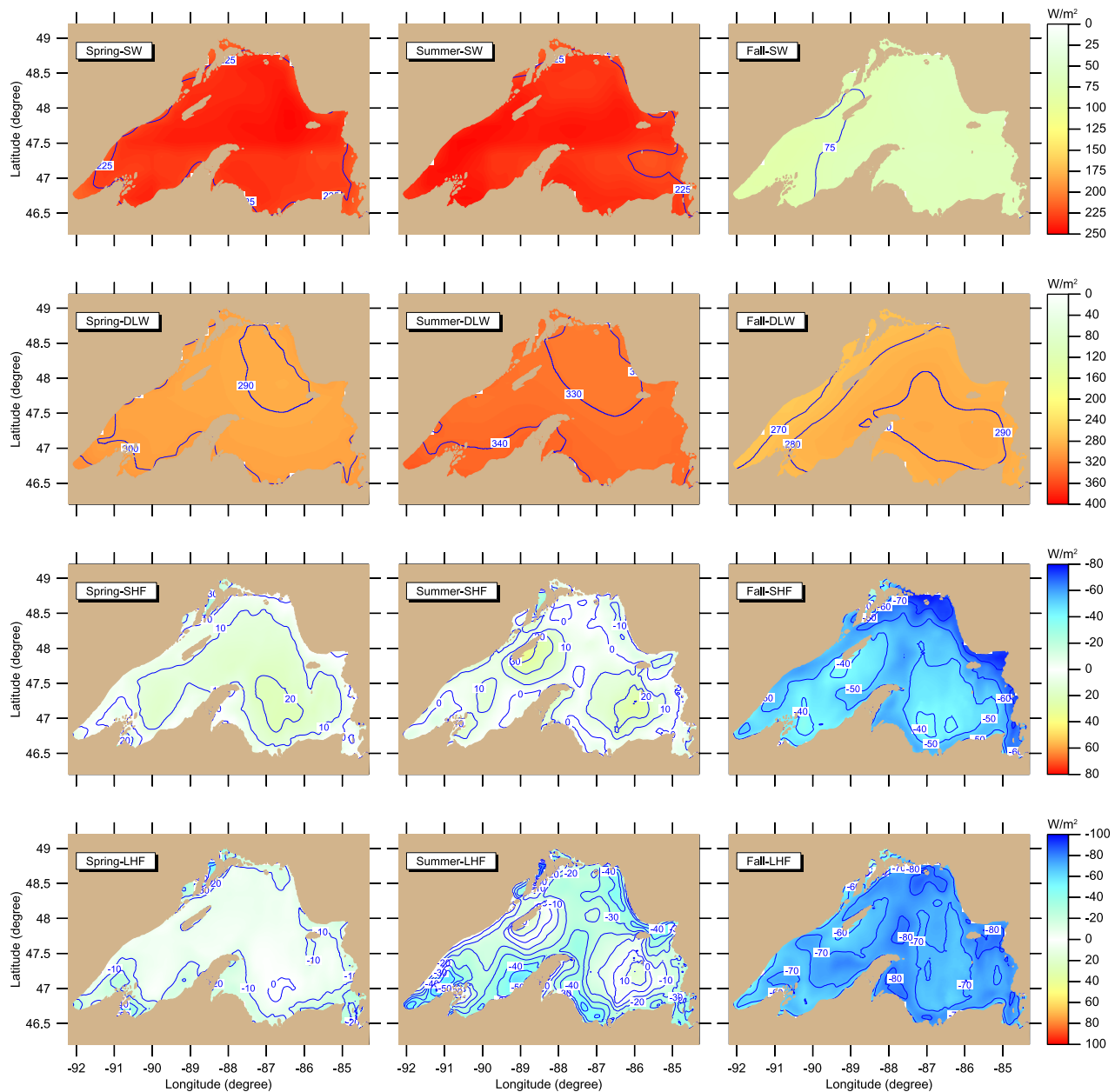


**Figure 12.** The spatial distribution of seasonal-mean surface heat fluxes during ice-free seasons in 2011: Shortwave radiation (SW), Downward longwave radiation (DLW), Sensible heat flux (SHF), and Latent heat flux (LHF) from case C2-III.

when interpolated spatially. The accurate simulation of the lake thermal structure also requires an accurate estimate of latent and sensible heat fluxes, which contain large spatiotemporal uncertainty and must be estimated in a higher resolution (e.g., dynamically calculated based on prognostic surface water temperature simulated within the model).

#### 4.4. Hybrid Forcing Configuration

The above analyses reveal that the CFSR reanalysis data to some degree combines the advantages of both observational data (radiation fields) and modeling forcing (wind fields), hence the simulation driven by CFSR forcing was capable of producing the best results among the six experiments. If this is true, a hybrid atmospheric forcing with “Observation-interpolated” solar radiation and downward longwave radiation along with “WRF-simulated” wind should directly take advantage of observational data and WRF wind for more accurate representation of the meteorological forcing (see Table 1). The model results with the hybrid

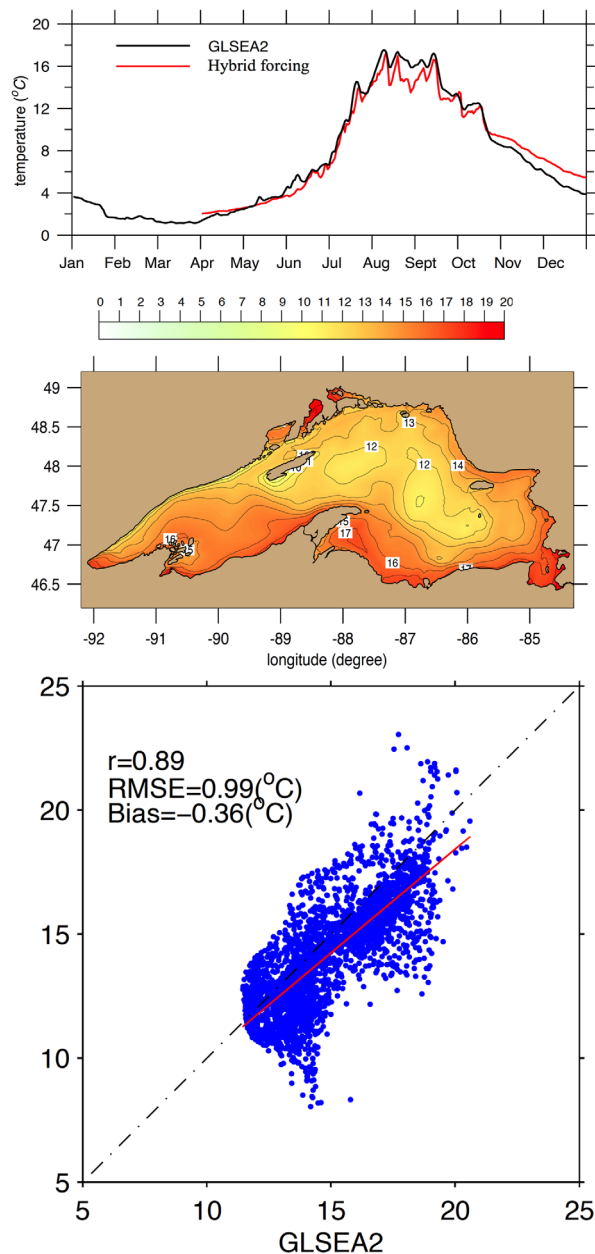


**Figure 13.** Model-data comparison for the case with hybrid forcing (see Table 1). (top) Time series of the lake-average surface water temperature; (middle) horizontal distribution of the summer surface water temperature; and (bottom) scatter plots of model-computed surface water temperature via GLSEA2 data sampled at 5 km resolution.

underlying dynamic explanations of the observed modeling success. The model with precomputed surface flux produces a significant cold bias due to inaccurate estimate of the surface heat flux. The latent and sensible heat fluxes are highly variable in space and time through direct interactions with meteorological variables and surface water temperature. Such strong variability can be resolved in a model when the fluxes are calculated dynamically based on the prognostic surface water temperature, as oppose to precomputing them with prescribed surface water temperatures. By implementing the dynamically computed heat flux algorithm in FVCOM to resolve the local lake-air feedbacks, the model produces more accurate estimates of the surface water temperature with average error < 1°C. Results also reveal that wind plays a critical role in controlling the spatial pattern of surface water temperature, particularly through the impact of wind speed on latent and sensible heat fluxes. The strong local variability of wind speed near the coastal transition zone

forcing proved to be even better than the best case (C2-III) that uses CFSR forcing (Figure 13). The model simulation improved in both simulated lake-average temperature (Figure 13, top) and the spatial pattern of surface water temperature (Figure 13, middle). This is further evidenced by the direct one-on-one comparison (Figure 13, bottom), which clearly shows not only the lowest RMSE of 0.99°C and bias of -0.36°C but also high correlation of 0.89 with individual points scattered well in line with the ideal fitting line. This reveals that the variability and interactions of the surface heat flux and the surface water temperature are well resolved by using the 3-D circulation model and an assimilative weather forecasting model. The model estimated surface heat fluxes in the hybrid case are summarized in Figure 14.

Although the lake circulation is not the primary focus in this study, a reliable model is expected to provide good simulations in general circulation patterns as long as surface forcings are properly configured. Figure 15 presents the modeled summer mean currents in the upper 20 m overlaid with the best-known schematic flow pattern from *Beletsky et al. [1999]* based on observations of summer 1967. The model-simulated general circulation pattern shows an excellent agreement with the observation-based schematic flow in both basin-wide and local finer scales, and further demonstrates the model skill in the hydrodynamic simulation for Lake Superior.

### 5. Summary and Conclusion

Using a hydrodynamic model, a weather forecasting model, and meteorological and hydrographic observations, we have investigated the impact of atmospheric forcing representation on modeling of the thermal structure of Lake Superior and explored the

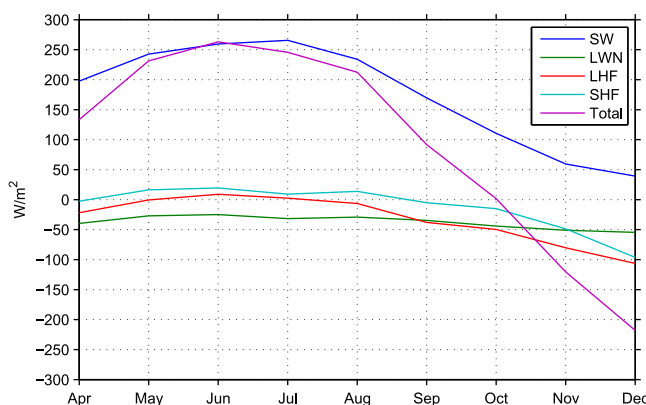


**Figure 14.** Monthly mean heat fluxes averaged over Lake Superior during ice-free months in 2011: Shortwave radiation (SW), net long-wave radiation (LWN), Sensible heat flux (SHF), Latent heat flux (LHF), and Total heat flux (Total).

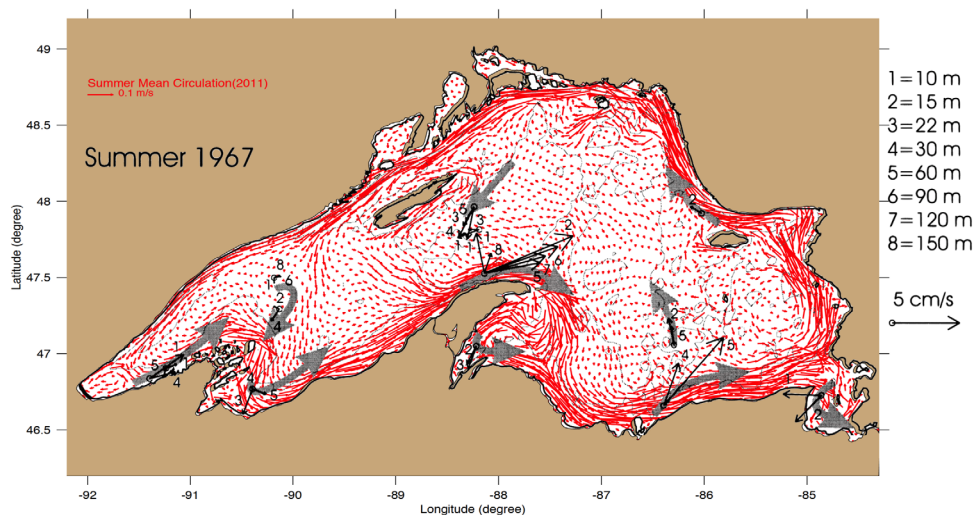


**Figure 15.** Model-simulated summer mean circulation (red) at upper 20 m for year 2011, overlaid with the schematic flow pattern (black) from [Beletsky et al., 1999] based on observations of summer 1967.

**Acknowledgments**

This is contribution 26 of the Great Lakes Research Center at Michigan Tech. Xue’s research was also supported by the U.S. Environmental Protection Agency grant GL00E01291-0 and the Michigan Tech Research Excellence Fund-Research Seed grant. The meteorological data used in this paper were retrieved through National Data Buoy Center (NDBC) <http://www.ndbc.noaa.gov/>. The NCEP CFSR reanalysis data are retrieved from <http://rda.ucar.edu/pub/cfsr.html>. The GLSEA2 data are produced at the NOAA Great Lakes Environmental Research Laboratory (GLERL) in Ann Arbor, Michigan through the NOAA CoastWatch program (<http://coastwatch.glerl.noaa.gov/glsea.html>). We thank Jay Austin (jaustin@d.umn.edu) for providing us the moored temperature observation and John Lenters for providing valuable comments on this paper. We also acknowledge anonymous reviewers’ comments and suggestions, which have greatly helped us to improve this research.

is found to be critical, and is well captured by the WRF model as opposed to the “observation-interpolated” wind. Downward radiative fluxes, however, can be well represented by observation-based spatial interpolation, due to the limited degree of spatial variability. Overall, this study reveals the role of spatially resolved lake-atmosphere interactions in modeling the hydrodynamics of Lake Superior and, in particular, the distribution of surface water temperature. We expect that further improvements will be achieved by developing a fully coupled lake-atmosphere model.

**References**

Anderson, E. J., and D. J. Schwab (2013), Predicting the oscillating bi-directional exchange flow in the Straits of Mackinac, *J. Great Lakes Res.*, *39*, 663–671.  
 Assel, A. A. (1990), An ice-cover climatology for lake Erie and lake superior for the winter seasons 1897–1898 to 1982–1983, *Int. J. Climatol.*, *10*, 731–748.  
 Austin, J. (2013), Observations of near-inertial energy in Lake Superior, *Limnol. Oceanogr.*, *58*, 715–728.  
 Austin, J. A., and J. Allen (2011), Sensitivity of summer Lake Superior thermal structure to meteorological forcing, *Limnol. Oceanogr.*, *56*, 1141–1154.  
 Austin, J. A., and S. M. Colman (2007), Lake Superior summer water temperatures are increasing more rapidly than regional air temperatures: A positive ice-albedo feedback, *Geophys. Res. Lett.*, *34*, L06604, doi:10.1029/2006GL029021.  
 Bai, X., J. Wang, D. J. Schwab, Y. Yang, L. Luo, G. A. Leshkevich, and S. Liu (2013), Modeling 1993–2008 climatology of seasonal general circulation and thermal structure in the Great Lakes using FVCOM, *Ocean Modell.*, *65*, 40–63.  
 Beardsley, R. C., C. Chen, and Q. Xu (2013), Coastal flooding in Scituate (MA): A FVCOM study of the 27 December 2010 nor’easter, *J. Geophys. Res. Oceans*, *118*, 6030–6045, doi:10.1002/2013JC008862.

- Beletsky, D., J. H. Saylor, and D. J. Schwab (1999), Mean Circulation in the Great Lakes, *J. Great Lakes Res.*, *25*, 78–93.
- Beletsky, D., D. Schwab, and M. McCormick (2006), Modeling the 1998–2003 summer circulation and thermal structure in Lake Michigan, *J. Geophys. Res.*, *111*, C10010, doi:10.1029/2005JC003222.
- Beletsky, D., N. Hawley, and Y. R. Rao (2013), Modeling summer circulation and thermal structure of Lake Erie, *J. Geophys. Res. Oceans*, *118*, 6238–6252, doi: 10.1002/2013JC008854.
- Bennington, V., G. A. McKinley, N. Kimura, and C. H. Wu (2010), General circulation of Lake Superior: Mean, variability, and trends from 1979 to 2006, *J. Geophys. Res.*, *115*, C12015, doi:10.1029/2010JC006261.
- Blanken, P. D., C. Spence, N. Hedstrom, and J. D. Lenters (2011), Evaporation from Lake Superior: 1. Physical controls and processes, *J. Great Lakes Res.*, *37*, 707–716.
- Chen, C., R. C. Beardsley, S. Hu, Q. Xu, and H. Lin (2005), Using MM5 to hindcast the ocean surface forcing fields over the Gulf of Maine and Georges Bank Region\*, *J. Atmos. Oceanic Technol.*, *22*, 131–45.
- Chen, C., R. C. Beardsley, and G. Cowles (2006), An unstructured grid, finite-volume coastal ocean model (FVCOM) system, *Oceanography*, *19*, 78–89.
- Chen, C., J. Zhu, E. Ralph, S. A. Green, J. W. Budd, and F. Y. Zhang (2001), Prognostic Modeling Studies of the Keweenaw Current in Lake Superior. Part I: Formation and Evolution, *J. Phys. Oceanogr.*, *31*, 379–395.
- Chen, C., Q. Xu, E. Ralph, J. W. Budd, and H. Lin (2004), Response of Lake Superior to mesoscale wind forcing: A comparison between currents driven by QuikSCAT and buoy winds, *J. Geophys. Res.*, *109*, C10502, doi:10.1029/2002JC001692.
- Clites, A. H., J. Wang, K. B. Campbell, A. D. Gronewold, R. A. Assel, X. Bai, and G. A. Leshkevich (2014), Cold water and high ice cover on Great Lakes in Spring 2014, *Eos Trans. AGU*, *95*, 305–306.
- Cotton, G. F. (1979), ARL models of global solar radiation, in *Hourly Solar Radiation-Surface Meteorological Observations*, vol. 2, *Final Rep. TD-9724*, SOLMET, Natl. Clim. Data Cent., Asheville, N. C.
- Dupont, F., P. Chittibabu, V. Fortin, Y. R. Rao, and Y. Lu (2012), Assessment of a NEMO-based hydrodynamic modelling system for the Great Lakes, *Water Qual. Res. J. Can.*, *47*(3–4), 198–214, doi:10.2166/Wqrj.2012.014.
- Fairall, C. W., E. F. Bradley, D. P. Rogers, J. B. Edson, and G. S. Young (1996), Bulk parameterization of air-sea fluxes for Tropical Ocean-Global Atmosphere Coupled-Ocean Atmosphere Response Experiment, *J. Geophys. Res.*, *101*, 3747–3764.
- Fujisaki, A., J. Wang, X. Bai, G. Leshkevich, and B. Lofgren (2013), Model-simulated interannual variability of Lake Erie ice cover, circulation, and thermal structure in response to atmospheric forcing, 2003–2012, *J. Geophys. Res. Oceans*, *118*, 4286–4304, doi:10.1002/jgrc.20312.
- Guttman, N. B., and J. D. Matthews (1979), Computation of extraterrestrial solar radiation, solar elevation angle, and true solar time of sunrise and sunset, in *Hourly Solar Radiation-Surface Meteorological Observations*, vol. 2, *Final Rep. TD-9724*, SOLMET, Natl. Clim. Data Cent., Asheville, N. C.
- Haidvogel, D. B. et al. (2008), Ocean forecasting in terrain-following coordinates: Formulation and skill assessment of the Regional Ocean Modeling System, *J. Comput. Phys.*, *227*, 3595–3624.
- Huang, A., Y. R. Rao, and Y. Lu (2010), Evaluation of a 3-D hydrodynamic model and atmospheric forecast forcing using observations in Lake Ontario, *J. Geophys. Res.*, *115*, C02004, doi:10.1029/2009JC005601.
- Ivanoff, A. (1977), Oceanic absorption of solar energy, in *Modelling and Prediction of the Upper Layers of the Ocean*, edited by E. B. Kraus, pp. 47–72, Pergamon, N. Y.
- Lam, D. C. L. (1978), Simulation of water circulations and chloride transports in Lake Superior for summer 1973, *J. Great Lakes Res.*, *4*, 343–349.
- Lenters, J. D., J. B. Anderton, P. Blanken, C. Spence, and A. E. Suyker (2013), Assessing the impacts of climate variability and change on Great Lakes Evaporation, in *2011 Project Reports*, edited by D. Brown, D. Bidwell, and L. Briley, Available from the Great Lakes Integrated Sciences and Assessments (GLISA) Center.
- Lofgren, B. M., and Y. Zhu (2000), Surface Energy Fluxes on the Great Lakes Based on Satellite-Observed Surface Temperatures 1992 to 1995, *J. Great Lakes Res.*, *26*, 305–314.
- Marchesiello, P., J. C. McWilliams, and A. Shchepetkin (2003), Equilibrium structure and dynamics of the California Current System, *J. Phys. Oceanogr.*, *33*, 753–783.
- Mason, E., F. Colas, J. Molemaker, A. F. Shchepetkin, C. Troupin, J. C. McWilliams, and P. Sangrà (2011), Seasonal variability of the Canary Current: A numerical study, *J. Geophys. Res.*, *116*, C06001, doi:10.1029/2010JC006665.
- Parkinson, C. L., and W. M. Washington (1979), A large-scale numerical model of sea ice, *J. Geophys. Res.*, *84*, 311–337.
- Penven, P., V. Echevin, J. Pasapera, F. Colas, and J. Tam (2005), Average circulation, seasonal cycle, and mesoscale dynamics of the Peru Current System: A modeling approach, *J. Geophys. Res.*, *110*, C10021, doi:10.1029/2005JC002945.
- Rao, Y. R., and D. J. Schwab (2007), Transport and mixing between the coastal and offshore waters in the Great Lakes: A review, *J. Great Lakes Res.*, *33*, 202–218.
- Røed, L., and J. Albretsen (2007), The impact of freshwater discharges on the ocean circulation in the Skagerrak/northern North Sea area Part I: Model validation, *Ocean Dyn.*, *57*, 269–285.
- Saha, S., et al. (2014), The NCEP Climate Forecast System Version 2, *J. Clim.*, *27*, 2185–2208, doi: http://dx.doi.org/10.1175/JCLI-D-12-00823.1.
- Sambridge, M., J. Braun, and H. McQueen (1995), Geophysical parametrization and interpolation of irregular data using natural neighbours, *Geophys. J. Int.*, *122*, 837–857.
- Schertzer, W. M. (1978), Energy Budget and Monthly Evaporation Estimates for Lake Superior, 1973, *J. Great Lakes Res.*, *4*, 320–330.
- Schwab, D. J., and K. W. Bedford (1994), Initial implementation of the Great Lakes Forecasting System: A real-time system for predicting lake circulation and thermal structure, *Water Pollut. Res. J. Can.*, *29*(2/3), 203–220.
- Schwab, D. J., G. A. Leshkevich, and G. C. Muhr (1992), Satellite measurements of surface water temperature in the Great Lakes: Great Lakes Coastwatch, *J. Great Lakes Res.*, *18*, 247–258.
- Schwab, D. J., W. P. O'Connor, and G. L. Mellor (1995), On the net cyclonic circulation in large stratified lakes, *J. Phys. Oceanogr.*, *25*, 1516–1520.
- Shore, J. A. (2009), Modelling the circulation and exchange of Kingston Basin and Lake Ontario with FVCOM, *Ocean Modell.*, *30*, 106–114.
- Seo, H., A. J. Miller, and J. O. Roads (2007), The Scripps Coupled Ocean-Atmosphere Regional (SCOAR) Model, with applications in the eastern Pacific Sector, *J. Clim.*, *20*, 381–402.
- Spence, C., P. D. Blanken, N. Hedstrom, V. Fortin, and H. Wilson (2011), Evaporation from Lake Superior: 2: Spatial distribution and variability, *J. Great Lakes Res.*, *37*, 717–724.
- Spence, C., P. D. Blanken, J. D. Lenters, and N. Hedstrom (2013), The importance of spring and autumn atmospheric conditions for the evaporation regime of Lake Superior, *J. Hydrometeorol.*, *14*, 1647–1658.

- Wang, J., X. Bai, H. Hu, A. Clites, M. Colton, and B. Lofgren (2012), Temporal and spatial variability of Great Lakes Ice Cover, 1973–2010\*, *J. Clim.*, *25*, 1318–1329.
- Wei, J., P. Malanotte-Rizzoli, E. B. Eltahir, P. Xue, and D. Xu (2013), Coupling of a regional atmospheric model (RegCM3) and a regional oceanic model (FVCOM) over the maritime continent, *Clim. Dyn.*, *43*, 1575–1594.
- White, B., J. Austin, and K. Matsumoto (2012), A three-dimensional model of Lake Superior with ice and biogeochemistry, *J. Great Lakes Res.*, *38*, 61–71.
- Wyrski, K. (1965), The average annual heat balance of the North Pacific Ocean and its relation to ocean circulation, *J. Geophys. Res.*, *70*, 4547–4559.
- Xu, D., and P. Malanotte-Rizzoli (2013), The seasonal variation of the upper layers of the South China Sea (SCS) circulation and the Indonesian through flow (ITF): An ocean model study, *Dyn. Atmos. Oceans*, *63*, 103–130.
- Xue, P., and E. A. B. Eltahir (2015), Estimation of the Heat and Water Budgets of the Persian (Arabian) Gulf Using a Regional Climate Model, *J. Clim.*, *28*, 5041–5062, doi:10.1175/JCLI-D-14-00189.1.
- Xue, P., C. Chen, P. Ding, R. C. Beardsley, H. Lin, J. Ge, and Y. Kong (2009), Saltwater intrusion into the Changjiang River: A model-guided mechanism study, *J. Geophys. Res.*, *114*, C02006, doi:10.1029/2008JC004831.
- Xue, P., E. A. B. Eltahir, P. Malanotte-Rizzoli, and J. Wei (2014), Local feedback mechanisms of the shallow water region around the Maritime Continent, *J. Geophys. Res. Oceans*, *119*, 6933–6951, doi:10.1002/2013JC009700.
- Zhao, L., C. Chen, J. Vallino, C. Hopkinson, R. C. Beardsley, H. Lin, and J. Lerczak (2010), Wetland-estuarine-shelf interactions in the Plum Island Sound and Merrimack River in the Massachusetts coast, *J. Geophys. Res.*, *115*, C10039, doi:10.1029/2009JC006085.
- Zhu, J., C. Chen, E. Ralph, S. A. Green, J. W. Budd, and F. Y. Zhang (2001), Prognostic modeling studies of the Keweenaw Current in Lake Superior. Part II: Simulation, *J. Phys. Oceanogr.*, *31*, 396–410.